

Vibrational Spectroscopy

YC Nitrogen-Functionalized Hydrothermal Carbon Materials by Using Urotropine as the Nitrogen Precursor

Jan Willem Straten,^[a] Philipp Schleker,^[a, b] Małgorzata Krasowska,^[a] Emmanouil Veroutis,^[b] Josef Granwehr,^[b] Alexander A. Auer,^[a] Walid Hetaba,^[c] Sylvia Becker,^[a] Robert Schlögl,^[a, c] and Saskia Heumann^{*[a]}

Abstract: Nitrogen-containing hydrothermal carbon (N-HTC) materials of spherical particle morphology were prepared by means of hydrothermal synthesis with glucose and urotropine as precursors. The molar ratio of glucose to urotropine has been varied to achieve a continuous increase in nitrogen content. By raising the ratio of urotropine to glucose, a maximal nitrogen fraction of about 19 wt% could be obtained. Decomposition products of both glucose and urotropine react with each other; this opens up a variety of possible reaction pathways. The pH has a pronounced effect on the reaction pathway of the corresponding reaction steps. For the

first time, a comprehensive analytical investigation, comprising a multitude of analytical tools and instruments, of a series of nitrogen-containing HTC materials was applied. Functional groups and structural motifs identified were analyzed by means of FTIR spectroscopy, thermogravimetric MS, and solid-state NMR spectroscopy. Information on reaction mechanisms and structural details were obtained by electronic structure calculations that were compared with vibrational spectra of polyfuran or polypyrrole-like groups, which represent structural motifs occurring in the present samples.

Introduction

The one-pot synthesis of carbonaceous materials by hydrothermal carbonization of biomass (e.g., carbohydrates, agricultural residues, wood crops) is a simple, cheap, nontoxic, environmentally friendly, and highly efficient method^[1] that is carried out in aqueous medium at mild temperatures, usually 130–250 °C, under self-generated pressure. It is a promising synthetic technique that provides novel carbon-based materials and allows good control of the morphology, chemical composition, and structure.^[2] Nitrogen-containing carbon-based materials

have gained attention for potential applications in industrial and environmental fields. These materials contain an abundance of functional groups that extend their field of application substantially, including soil enrichment,^[3] as electrocatalysts in fuel cells (electrocatalysis),^[4] or as electrode materials for rechargeable batteries^[5] and supercapacitors^[6] (energy storage). Hydrothermal carbonaceous materials (HTCs) are also suitable for CO₂ capture^[7] and hydrogen storage^[8] (gas storage). Furthermore, nitrogen-containing HTCs (N-HTCs) can, among other applications, act as pH adsorbents; this means that they are promising candidates for utilization as sorption materials (purifiers) for water purification to remove heavy metals (e.g., Pb²⁺, Cd²⁺, Cu²⁺, U⁶⁺)^[9] or organic pollutants (e.g., dyes)^[10] from wastewater due to their abundance of surface functional groups. By variation of the pH value, the binding capacity, and therefore, selectivity, for a certain heavy metal could be increased. Also, the removal of an organic dye pollutant from water can be achieved at a certain pH range. HTCs also serve as chemical^[11] or gas sensors.^[12] Medical applications are found in the field of drug delivery^[13] or bioimaging.^[14]

The hydrothermal carbonization process is spontaneous and exothermic. Approximately one-third of the combustion energy remains in the hydrocarbon; hence the final energy stored in carbonized glucose (G)-based biomass is around 2200 kJ mol⁻¹.^[15] With the introduction of nitrogen, carbon materials show enhanced stability towards degradation,^[16] higher conductivity,^[17] and improved electrochemical characteristics, as well as enhanced binding capacities towards nanoparticles for higher catalytic activity.^[6a, 18]

[a] J. W. Straten, Dr. P. Schleker, Dr. M. Krasowska, Prof. Dr. A. A. Auer, Dr. S. Becker, Prof. Dr. R. Schlögl, Dr. S. Heumann
Max Planck Institute for Chemical Energy Conversion
Stiftstraße 34–36, 45470 Mülheim an der Ruhr (Germany)
E-mail: saskia.heumann@cec.mpg.de

[b] Dr. P. Schleker, E. Veroutis, Prof. Dr. J. Granwehr
Forschungszentrum Jülich, IEK-9, Wilhelm-Johnen Straße
52425 Jülich (Germany)

[c] Dr. W. Hetaba, Prof. Dr. R. Schlögl
Fritz Haber Institute of the Max Planck Society
Faradayweg 4–6, 14195 Berlin (Germany)

Supporting information and the ORCID identification numbers for the authors of this article can be found under <https://doi.org/10.1002/chem.201800341>.

© 2018 The Authors. Published by Wiley-VCH Verlag GmbH & Co. KGaA. This is an open access article under the terms of Creative Commons Attribution NonCommercial License, which permits use, distribution and reproduction in any medium, provided the original work is properly cited and is not used for commercial purposes.

Part of a Special Issue to commemorate young and emerging scientists. To view the complete issue, visit Issue 47.

Herein, we report the synthesis of nitrogen-functionalized carbonaceous materials by hydrothermal treatment by using G as a carbon source and urotropine (Uro) as a nitrogen source. Overall, three different structure models were proposed for HTC chars to describe nitrogen-free (N: 0 wt%), highest nitrogen content (N: 19 wt%), and lowest nitrogen content (N: 7 wt%) with the aid of spectrometric and spectroscopic methods.

Results and Discussion

Precursor decomposition and mechanistic aspects of condensation chemistry

The N-HTC was synthesized with G and Uro as precursors. Their decomposition and possible reaction pathways are briefly discussed. The pathway in the acyclic configuration to the direct formation of 5-hydroxymethyl furfural (HMF) by acid-catalyzed dehydration of hexoses (e.g., G) is widely known.^[19] Decomposition of the monosaccharide G occurs most likely through initial acid-^[19a] or base-catalyzed^[20] aldose–ketose isomerization (Lobry de Bruyn–Alberda van Ekenstein transformation), followed by three dehydration steps, forming the intermediate HMF.^[19a] HMF can further decompose after several steps into levulinic acid and formic acid. The described decomposition is illustrated in Figure S1 b in the Supporting Information.^[21] The decomposition process also includes a variety of side reactions, leading, for the most part, in liquid fuel and chemical production, to undesired polymeric byproducts called humins.^[19a,21a,22]

Several reaction pathways occur during the decomposition of the initial reactant G.^[17a,19a] Considering the decomposition products of G, as well as ammonia and formaldehyde as additional reagents derived from Uro, several N-containing structural motifs can be formed based on retrosynthetic ideas (Figure 1 and Figure S2 and Table S1 in the Supporting Information). The decomposition processes of both precursors open up a multitude of possible reaction pathways in the presence of ammonia that are discussed below.

The introduction of nitrogen into the carbon network during hydrothermal treatment is not fully understood. It is accepted that the Maillard reaction is one of the reaction pathways taking place in the presence of amine compounds or amino acids.^[17a,23] Briefly, it includes amination, imination (Schiff base), Amadori rearrangement, cyclization (cyclic/heterocyclic compounds), transformation into aromatic motifs (e.g., pyrazine, pyrrole, pyrone, furan), and further degradation reactions (Strecker degradation).^[17a,23b,24] However, it prefers to occur between reducing sugars (e.g., G) and amino acids. Reducing sugars in aqueous medium are stable over the range of pH 5–7. Nevertheless, this changes in more acidic and alkaline environments or in the presence of amine compounds.^[23d] With increasing acidities, the degradation of G is characterized by slow enolization due to unfavorable protonation of the carbonyl group. Subsequent water elimination occurs rapidly. The intermediate of this decomposition process is 3-deoxygluco-

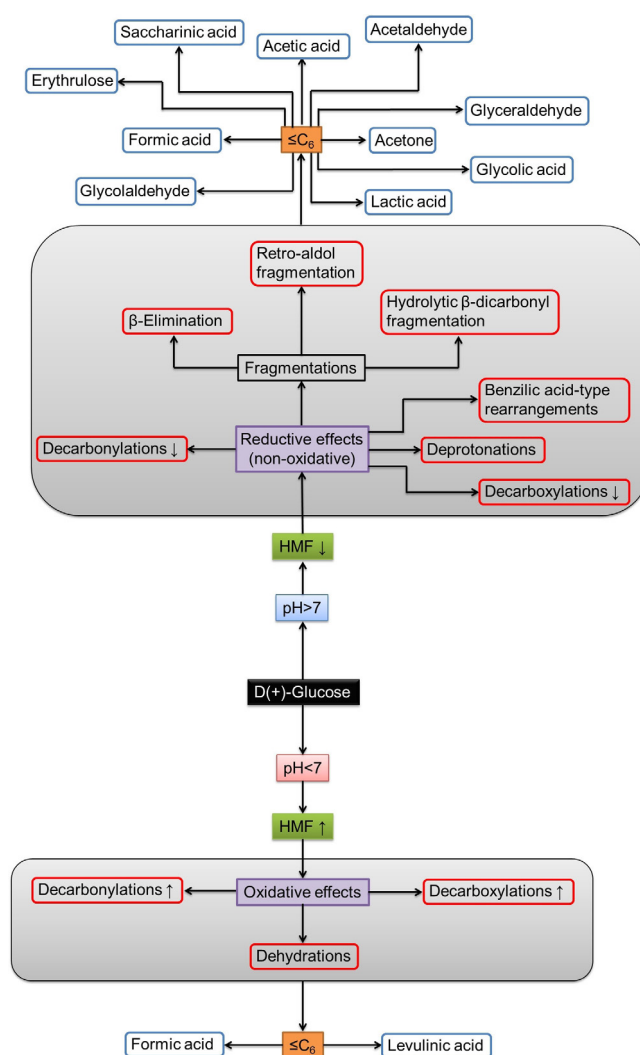


Figure 1. Schematic illustration of the pH-dependent synthetic pathways and their reaction mechanisms resulting in $\leq C_6$ decomposition products.

some if G is used as starting material. Further dehydration, cyclization, and aromatization yields HMF.^[23d]

Both acid- and base-catalyzed decomposition processes are observed during hydrothermal synthesis with G.^[19a,20,23d] In an

Saskia Heumann received her Ph.D. in chemistry in 2012 from the Christian-Albrechts University of Kiel, Germany. Afterwards, she moved to the Max Planck Institute for Chemical Energy Conversion (MPI CEC) as Group Leader in the Department of Heterogeneous Reactions. Together with her “Carbon Synthesis and Applications” group, she investigates carbon-based (electro)catalysts. She is interested in the synthesis and modification of carbon materials, tethering techniques of heteroatoms and their characterization, with a focus on the investigation of structure–property correlations. The catalytic materials are explored in the field of energy storage.



alkaline environment, the degradation of hexoses (e.g., G) results in numerous lower molecular weight acidic products of $\leq C_6$ compounds (Figure S1 b in the Supporting Information). The C_6 acidic compounds include deoxyaldonic acids (saccharinic acids).^[20a,23d,25] Byproducts such as higher molecular weight acidic compounds of $> C_6$ acids, as well as nonacidic and cyclic unsaturated carbonyl compounds, are also identified to a lesser extent.^[20a,26] At $pH > 11$, the reaction pathway via HMF is suppressed.^[20b] Instead, the concentration of lactic acid, acetic acid, and acetaldehyde increases significantly, which means that the reaction pathway via glyceraldehyde plays an important role in alkaline environments.^[20b] Under alkaline conditions, the main products are glycolic acid and acetone (Figure S1 b in the Supporting Information). Glycolaldehyde has also been ascertained as a considerable product.^[20b,27] After β -elimination of 2,3-enediol, keto-enol tautomerization can be followed by conversion into an α -dicarbonyl, which further reacts to form glycolic acid and 3-hydroxybutanal. Subsequent dehydration, keto-enol tautomerization, and retro-aldol fragmentation of 3-hydroxybutanal forms formic acid and acetone.^[20b] Under alkaline conditions, enolization occurs considerably faster due to the pronounced C-H acidity and greater availability of carbonyl groups in the open-chain form. Nonetheless, enolization occurs throughout the whole sugar chain. For instance, the psicose can be formed via 2,3-enediol, which has an effect on all further decomposition reactions because it can lead to undesirable byproducts (Figure S1 b in the Supporting Information).^[23d] The comparatively easier enolizability creates conditions for β -elimination reactions. Starting from 1,2-enediol, cleavage of a water molecule can lead to the formation of 3-deoxyglucosone (α -dicarbonyl) or 2,3-enediol and to the generation of 1-deoxyglucosone (α -dicarbonyl; Figure S1 b in the Supporting Information). Thus, the dehydration reactions of all enediol structures yield α -dicarbonyl compounds, which are deoxy sugars.^[23d] For more detailed reaction mechanisms occurring in alkaline environments, see Figures S3–S5 in the Supporting Information.

It has to be taken into account that it is not possible to define a certain mechanism for the formation of a N-HTC due to the complexity of the decomposition process during hydrothermal synthesis.^[17a,28] Also, various other non-Maillard reaction mechanisms occur simultaneously to form N-HTCs, including Diels–Alder cycloaddition or imino-Diels–Alder reactions, resulting in the formation of heterocycles.^[9a,17a,29]

Both starting materials for the synthesis of N-functionalized HTC, G and Uro, are dissolved in aqueous medium, transferred to Teflon-lined autoclaves, and treated hydrothermally at tem-

peratures up to 180 °C for 6 h. As a byproduct, a liquid supernatant is formed (Figure 2). Under these hydrothermal synthesis conditions Uro presumably decomposes into formaldehyde and ammonia (Figure S1 a in the Supporting Information),^[30] which are able to react with the decomposition products of G (Figure S1 b in the Supporting Information).

Carbon materials of spherical particles are obtained with maximal nitrogen contents of 19 wt%, which far exceeds the nitrogen content obtained through other synthetic procedures.^[17a] Our group previously reported the role of synthetic pH on the properties of HTCs in terms of specific functionalization, powder density, morphology, particle size, and color change.^[31] Because the addition of N-precursor also increases the synthetic pH, herein pH-dependent structural changes are discussed. The liquid supernatant as a byproduct was investigated with regard to molecular compounds and acid–base characteristics. As mentioned previously, some reaction pathways (pyrrole vs. furan syntheses) occur in preferential pH regimes. Furthermore, the reaction parameters, such as temperature, play a major role on the potential reaction pathways. At high temperatures applied for the preferential production of carbonaceous products, inevitably, multiple types of reactions occur simultaneously, such as cyclization, imination, amination, or condensation reactions, in which both cross-linking and N-doping occur.^[17a]

Because polyfuran or polypyrrole groups are prominent structural entities, further information of structural motifs and their properties has been obtained by electronic structure calculations of model systems.

Two systematic series of HTCs were synthesized in autoclaves from pure G and from a mixture of G and Uro at different molar ratios. In the first series, only the concentration of G was modified; the amount of Uro was unchanged. Molar ratios of G/Uro of 1:0.17, 1:0.2, 1:0.25, 1:0.33, 1:0.5, and 1:1 were prepared. In the second series, only the mass fraction of Uro was changed; the content of G was kept constant. Molar ratios of G/Uro of 1:2, 1:3, and 1:4 were synthesized. The G/Uro reaction solutions before hydrothermal treatment and the colored liquid supernatants obtained after hydrothermal synthesis were tested for their pH (Figure 3 and Table S2 in the Supporting Information). Likewise, the ratios of C/N and C/H as functions of the N content were determined.

The pH values of the initial solutions increase slightly with increasing Uro concentrations from $pH \approx 8$ to 9, in comparison with the solution of pure G, which has $pH \approx 5$. On the other hand, the pH values after synthesis, which were determined by rehydration products of HMF, such as levulinic acid, formic acid, and acetic acid, showed a drastic drop at the pivot point at which the G/Uro ratio reversed (Figure 3a). Consequently, other reaction pathways and carbon formation processes take place. The ratios of C/N and C/H decrease considerably with higher N content (Figure 3b). The N-HTCs showed color variations that depended on the molar ratio of G/Uro (Table S3 in the Supporting Information); these are discussed in detail in the next section. Briefly, for samples with a brown to dark brown color (1:4–1:1 G/Uro), similar C/N values of 3.7–3.1 and C/H values of 10.6–9.3 are obtained. There is a turning point at

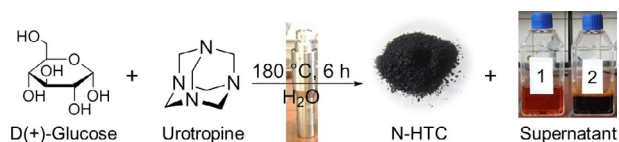


Figure 2. General reaction scheme for the hydrothermal synthesis of N-HTC (main product) and liquid supernatant (byproduct) from G and Uro. The liquid supernatant of pure G has an orange–red color (1), whereas the mixture of the supernatant of G and Uro has a dark brown color (2).

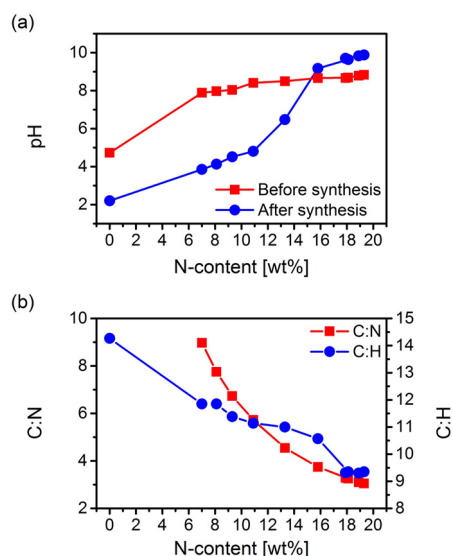


Figure 3. a) The pH values of the liquid supernatant of the G/Uro reaction solution before and after hydrothermal synthesis. The pH values are plotted against the molar ratio of Uro normalized to G. b) Ratios of C/N and C/H as a function of the N content.

which the sample starts to turn black (1:0.5 G/Uro). At this point, not only the ratios of C/N and C/H start to increase, but also the pH value becomes more acidic. The N-free HTC shows an acidic pH of 2.2 and, at the same time, exhibits quite a high C/H ratio of 14.3. At lower pH values, as the HTC starts to turn from brown into black, it changes to a more extensive degree of internal condensation of the polymeric carbonaceous network, and therefore, an increasing amount of cross-linking bonds is observed. This phenomenon was observed previously in the context of initial synthetic pH studies of HTCs.^[31]

UV/Vis spectroscopy

The materials synthesized at high Uro mass fractions (1:4–1:3 G/Uro) reveal a brown color that turns into a dark brownish shade (1:2–1:1 G/Uro) before becoming completely black (1:0.5–1:0.17 G/Uro). Nevertheless, a pure HTC (1:0 G/Uro) has a brown color. Four of these colorful N-HTCs (1:1, 1:1.5, 1:3 and 1:4 G/Uro) were subjected to UV/Vis spectroscopic measurements (Figures S6–S10 in the Supporting Information). The UV/Vis spectra of N-HTCs exhibit a maximum between $\lambda = 325$ and 380 nm in the blue to violet–UV region of the electromagnetic spectrum, which resembles a semiconductor band gap in the region of 2.0–2.2 eV.^[32] In contrast, graphitic carbon nitride ($g\text{-C}_3\text{N}_4$) has a band gap of approximately 2.7 eV.^[33] Upon applying Kubelka–Munk functions and Tauc plots, similar intrinsic band gaps are obtained that range from 1.7–1.8 to 1.9–2.0 eV, respectively (Table S4 in the Supporting Information). In each case, the N-HTC with lowest N content exhibits the smallest band gap; with increasing N content the band gap increases, which suggests a trend that a higher N content results in brighter color of the N-HTC and a larger band gap. Increasing the N content to 19 wt% resulted in the absorption edge shifting to slightly shorter wavelengths. The additional absorption

band at $\lambda \approx 400\text{--}500$ nm underlines the characteristic of the N-HTCs absorbing at wavelengths in the visible range.^[32a] The absorption band at $\lambda = 250$ nm can be ascribed to the $\pi \rightarrow \pi^*$ electronic transition in an aromatic 1,3,5-triazine-like compound.^[32b,34] However, this statement and the following interpretations should be treated with caution because the assignments refer to $g\text{-C}_3\text{N}_4$.^[32,34] The intense band at $\lambda = 325\text{--}380$ nm can be attributed to $\pi \rightarrow \pi^*$ transitions present in N-containing conjugated aromatic ring systems, for example, heterocyclic aromatics.^[32] At $\lambda \approx 400\text{--}500$ nm, the absorption band can be assigned to $n \rightarrow \pi^*$ transitions, including lone pairs of N atoms of aromatic rings.^[32,34c]

HPLC

HPLC measurements confirm the presence of fructose, HMF, and levulinic and formic acids (Figure S11 in the Supporting Information). Increasing amounts of formic acid and decreasing concentrations of acetic acid can be observed with increasing amounts of Uro, as depicted in Figure 4 (Figure S12; for abso-

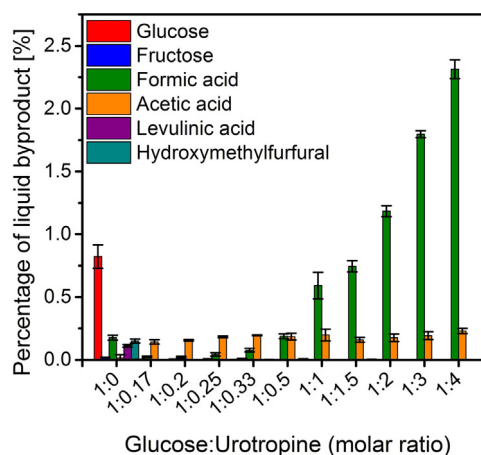


Figure 4. Percentage of liquid byproducts in the supernatant, normalized to initial G concentration, as a function of the molar ratio between G and Uro, as determined by HPLC.

lute values, see Tables S5 and S6 in the Supporting Information). The HMF band is only visible if pure G is used as a starting material and if G itself is completely consumed in the case of high G/Uro ($G/Uro > 1:0.5$) ratios. The complex chromatogram indicates that byproducts other than levulinic and formic acid are present in the liquid phase after rehydration.

An increase in the amount of acidic byproduct in the supernatant with increasing molar ratio of Uro/G was observed by HPLC. At first glance, this is in contradiction to the pH measurements, which show a higher basicity as the amount of Uro to G increases. The decomposition of Uro is driven thermodynamically and through acid or base catalysis, yielding decomposition products of formaldehyde and ammonia.^[35] Formaldehyde itself is oxidized and converted into formic acid. Ammonia ($pK_b = 4.75$, strong base) leads, in total, to an increase in ba-

sitivity of the supernatant, and thus, suppresses the acidity of formic acid ($pK_a=3.75$, strong acid), acetic acid ($pK_a=4.75$, medium-strong acid), and levulinic acid ($pK_a=4.78$, medium-strong acid). With a higher molar ratio of Uro/G, more formic acid catalyzes the decomposition of Uro, which increases the concentration of ammonia. According to the HPLC chromatogram, a higher percentage of formic acid remains after hydrothermal synthesis only at higher molar ratio of Uro/G. Due to the higher pH, it is likely that consecutive reactions involving formic acid are prevented. However, compounds with more basic behavior, such as ammonia or amine, could not be separated by the HPLC column. The HPLC column used for this application is only able to separate monosaccharides in combination with organic acids, fatty acids, alcohols, ketones, neutral compounds, or inorganic salts.

Macro- and microscopic morphology of N-HTCs

SEM and TEM images reveal the spherical morphology of the obtained N-HTCs (Figure 5). Moreover, all HTCs exhibit regions of aggregated particles. Particle sizes were determined from optical microscopy images after the materials were pressed into pellets (Figure S14 in the Supporting Information). The average particle size is around 3 to 6 μm for the N-HTCs, with a broader particle size distribution for samples with a higher G content. In comparison, pure HTC particles are smaller by a factor of 10, with an average particle size of 0.34 μm (Figures S13 and S14 and Table S7 in the Supporting Information). This change in particle size can be attributed to different kinds of mass fractions of the reactants used, as well as the increased complexity of possible reaction pathways by adding Uro to

form a variety of organic compounds, as mentioned in the Introduction. Growth of the carbon microspheres occurs according to the LaMer model.^[36] Through the polymerization and cross-linking processes, first, species form nuclei followed, by spherical growth.^[36,37] Because the reactions occur in quite a complex manner inside the autoclave, polydisperse and agglomerated spherically shaped particles, rather than monodisperse particles are formed.^[1b] The LaMer model does not take the pH behavior into account, which is crucial for the decomposition behavior of the reactants used (Figures S1 and S2 in the Supporting Information). Recent pH-dependent studies on HTCs investigated the influence of the initial pH from pH 0 to 6, and revealed a change in particle size from 15 to 0.5 μm , respectively.^[31] At lower pH values, as the HTC starts to turn from brown into black, the formed carbons have a higher degree of internal condensation of the polymeric carbonaceous network, and therefore, an increasing amount of cross-linking bonds. Through hydrothermal synthesis of a basic pH amino sugar, such as glucosamine, smaller particle sizes than those of a pure G sample have been obtained.^[38] The addition of a basic comonomer, such as ethylenediamine, not only has an impact on the particle size, which decreases, but also, depending on the concentration of ethylenediamine, results in the morphology changing abruptly into a net/cross structure.^[39]

Specific surface areas were determined by nitrogen adsorption experiments and BET analysis. The synthesized N-HTCs provide negligibly small surface areas below $1\text{ m}^2\text{g}^{-1}$; pure HTC has a larger specific surface of around $9\text{ m}^2\text{g}^{-1}$ (Table S8 in the Supporting Information).

The structural texture of the N-HTCs was investigated by means of high-resolution (HR) TEM (Figure 6). In the outer part

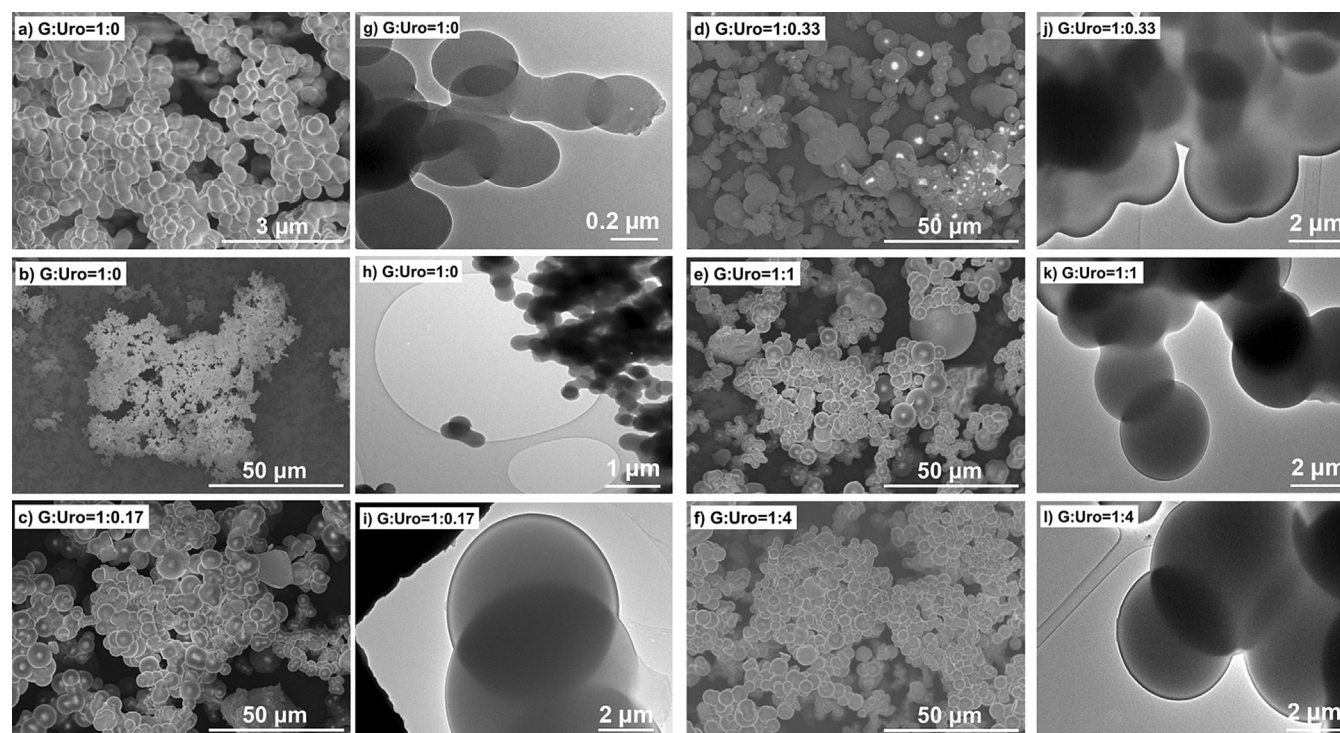


Figure 5. SEM (a–f) and TEM (g–l) images of N-HTCs with different compositions to illustrate spherical particle shapes.

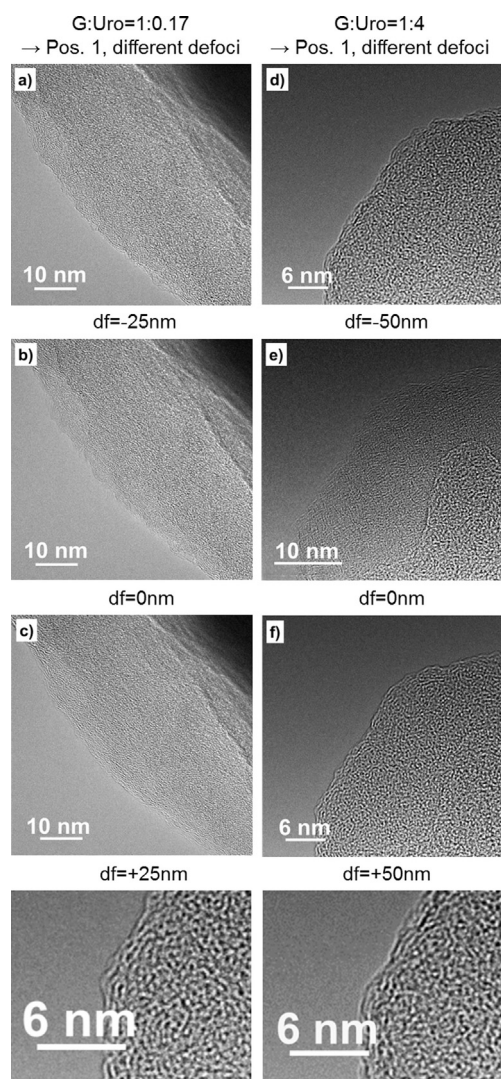


Figure 6. HRTEM images of N-HTCs with 1:0.17 (a–c) and 1:4 (d–f) G/Uro, obtained by applying different defocus (df) values. The bottom row shows cropped HRTEM images to highlight the isotropic of carbon structures.

of the carbon sphere surface, walls depict a surface roughness that can be accounted for by the irregular arrangement of 8–12 curved atom chains (e.g., C) caused by defect sites (e.g., O, N). As a result, there is no preferred direction. The highly curved texturing profile leads to isotropic orientation of the carbon structure.^[23c,40]

Elemental composition and yields

The determination of the elemental composition of the N-HTC samples was carried out by total organic carbon (TOC) combustion analysis. The results (in wt%) of different molar ratios of G/Uro are visualized in Figure 7 (Figure S15 in the Supporting Information). The absolute values are summarized in Table S9 in the Supporting Information. With increasing molar ratio of Uro/G, a maximal N content of about 19 wt% can be achieved with a simultaneous decrease in the C and O fractions.

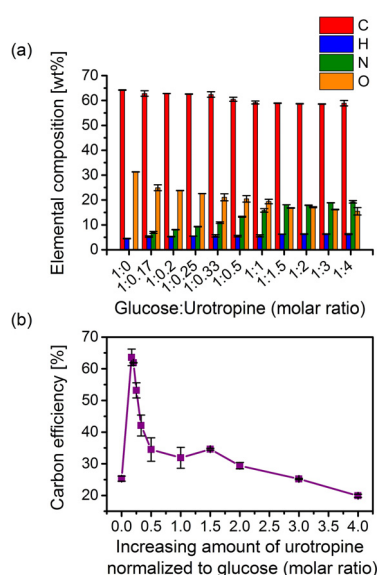


Figure 7. a) Elemental composition plotted versus the molar ratio of G/Uro and b) carbon efficiency of all synthesized HTC samples as a function of the increasing amount of Uro normalized to G.

It should be noted that standard deviations were calculated from at least two experiments running separately, with the same molar ratios of G/Uro. Oxygen was calculated by subtracting the amount of carbon, hydrogen, and nitrogen from 100%.

The carbon efficiency^[24b] was determined by using Equation (1):

$$\text{carbon efficiency [\%]} = \frac{\text{amount carbon in solid after hydrothermal synthesis [g]}}{\text{initial amount carbon in the reactants [g]}} \quad (1)$$

If only G is used as a starting material, the carbon efficiency is very low at around 25%, which is consistent with the high G peak in the HPLC experiments. A maximum carbon efficiency of approximately 64% could be achieved with the lowest amount of Uro to G under the applied synthetic conditions. Carbon loss can be explained by the transformation of G into degradation products, for example, levulinic, acetic, and formic acid or dihydroxyacetone, which is also in accordance with the HPLC measurements. The formation of liquid supernatant (liquefaction) and volatile side products (gasification), which are concurrent parallel reactions to the formation of HTC, are formed to a greater or lesser extent, depending on the preferential synthetic pathway.^[41] Furthermore, higher pH of the solvent is unfavorable for the internal degree of condensation because Uro very quickly releases ammonia if the pH rises too high and too fast (Figure 1). The reaction conditions at high Uro concentration favor fragmentation reactions over condensation reactions. Alternatively, more stable nitrogen sources or nonaqueous polar reaction medium could be applied for the hydrothermal synthesis.

Structural composition of N-HTCs

The structural compositions of N-HTCs were investigated by spectroscopic methods supported by electronic structure calculations. FTIR spectroscopy was performed in attenuated total reflection (ATR) mode. The collected spectra are shown in Figure 8 and Figure S16 in the Supporting Information.

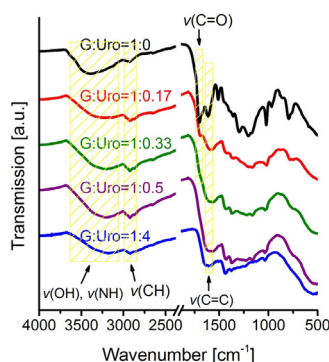


Figure 8. FTIR (ATR) spectra of the synthesized HTC samples with different molar ratios of G to Uro. Higher G to Uro ratio is depicted on top and higher Uro to G ratio below.

The broad absorption band between $\tilde{\nu}=3650$ and 3060 cm^{-1} corresponds to $\nu(\text{O-H})$ and $\nu(\text{N-H})$ stretching vibrations. Overlap of both functional groups prevents their exact determination. The aliphatic methylene-type $\nu(\text{C-H})_{\text{stretch}}$ is observed at $\tilde{\nu}\approx 2923\text{ cm}^{-1}$ for all synthesized materials. The $\nu(\text{C=O})$ band at $\tilde{\nu}=1700\text{ cm}^{-1}$ is only visible at higher molar ratios of G/Uro, starting from 1:0.33 G/Uro. The carbonyl group can probably be ascribed to a higher degree of internal condensation of the polymeric carbonaceous network structures because these HTC chars are characterized by acidic pH behavior, a higher HTC yield, and a higher carbon efficiency; thus, these materials are compact and robust. The band between $\tilde{\nu}=1630$ and 1550 cm^{-1} is attributed to the $\nu(\text{C=C})_{\text{stretch}}$ vibration, which indicates graphitic structures in the HTCs. Evaluation of the bands in the fingerprint region becomes more complicated. Theoretical studies of the IR spectra of carbon materials were carried out by Fuente and co-workers for different O-functional groups (carboxyl, lactone, anhydride, phenol, quinone, and pyrone) that were suitable for describing the surface chemistry of graphene layers.^[42] To the best of our knowledge, no efforts have been made so far to calculate IR spectra of HTCs, especially in the fingerprint region, because the exact structure of the HTC remains unclear. In the fingerprint region, however, it is only known that, for pure HTCs originating from xylose, highly intense bands at $\tilde{\nu}=880$ and 752 cm^{-1} ($\delta(\text{C-H})_{\text{oop}}$) stem from aromatic structural motifs.^[40,43]

Interpretation of the vibrational and deformation modes at these lower wavenumbers is supported by utilizing polyfuran and polypyrrole as model compounds for quantum-chemical calculations because oligomeric ring structures, such as polyfuran, were successfully verified to be a major part of the struc-

tural motifs of the HTC network.^[23b,24a-c] In terms of N-functionalization, it was proven that polypyrrole was an important structural motifs^[23b] and hexameric pyrrole was therefore chosen, in addition to hexameric furan, for calculations. For details on the electronic structure calculations, see the Supporting Information.

For a series of model compounds, such as hexameric furan and hexameric pyrrole, features of the vibrational spectra were evaluated by normal-mode analysis using DFT methods (Figures S17 and S18 in the Supporting Information).

Vibrational spectra of α -oligofurans and N-free HTC (pure HTC originating from G)

To assess the quality of simulated spectra for a well-characterized compound, the vibrational spectrum of furan was computed. Calculated harmonic vibrational frequencies of furan scaled by 0.97 are in good agreement with the experimentally obtained gas-phase spectrum (Figure S19 in the Supporting Information). It is known that HTC networks contain polyfuran motifs.^[23b,24a-c] Linear oligofurans containing two to six furan rings were chosen as model compounds that were assumed to match with furanic-type structural units to assess their agreement with calculated spectra (Figure 9). How accurately the IR

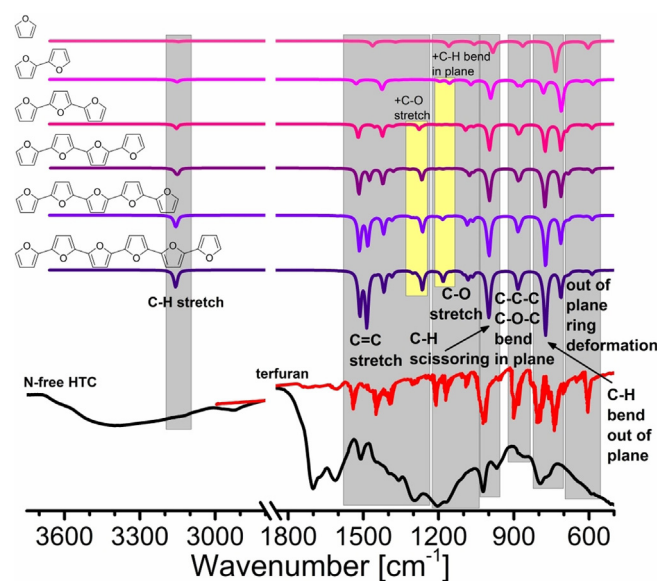


Figure 9. Computed (B3LYP-D3/def2-TZVP) IR spectra of linear oligofurans (one to six furan units, see schemes), experimental spectrum of terfuran^[44] (red line), and experimental FTIR spectrum of N-free HTC (black line). IR spectra are divided into regions according to the type of vibrations. Additional lines that appear jointly with the main vibration are marked with yellow boxes.

spectra of HTCs could be described by polyfuranic models and what influence the number of furan rings in α -oligofurans had on their vibrational spectra was then investigated. Additionally, the experimental IR spectrum of terfuran (Figure 9, red line)^[44] was compared with the computed spectra of α -oligofuran models and with the IR spectrum of N-free HTC (black line).

Theoretical vibrational spectra of furan and α -oligofurans can be divided into seven regions, according to the type of vibration they represent: out-of-plane ring deformation ($\tilde{\nu} < 700 \text{ cm}^{-1}$), C–H out-of-plane bending ($\tilde{\nu} \approx 680\text{--}820 \text{ cm}^{-1}$), C–C and C–O–C in-plane bending ($\tilde{\nu} \approx 820\text{--}920 \text{ cm}^{-1}$), C–H scissoring, C–O stretching, aromatic C=C stretching, and aromatic (or sp^2) C–H stretching. Increasing the number of furan rings influences the vibrational spectra of α -oligofurans considerably. Additional bands appear in the spectrum of 2,2'-bifuran, compared with the spectrum of furan, and the corresponding bands shift or their intensities change. Two or more types of vibrations can be assigned to some of the bands. An increased number of furan rings causes, for instance, the band corresponding to C–O–C out-of-plane bending to shift from $\tilde{\nu} = 603$ (furan) to $615\text{--}630 \text{ cm}^{-1}$ (hexameric furan) and its intensity significantly decreases. Additionally, two other bands appear: one at $\tilde{\nu} \approx 590 \text{ cm}^{-1}$, with a very low intensity, that represents out-of-plane C–C–C ring deformation, and another one at $\tilde{\nu} \approx 680\text{--}690 \text{ cm}^{-1}$ (depending on the oligomer length), which is described by the combination of C–O–C bending with asymmetric C–H out-of-plane bending. In the region of C–H out-of-plane bending, a further band occurs. This band corresponds to C–H out-of-plane bending of inner furan rings and its intensity increases with increasing number of rings. The lower lying band in this region corresponds to the C–H out-of-plane bending in the two outer furan rings. The intensity of the bands in the regions of in-plane ring bending and C–H scissoring increases as the oligofuran chain is elongated. In the wider regions of aromatic C=C and C–O stretching, more new bands appear that grow in intensity. These are mainly the combinations of symmetric and asymmetric bond stretches of individual rings and other vibration types, that is, C–H in-plane bending in the case of bands in the region of C–O stretching or a mixture of C=C and C–O stretching in the C=C stretching region. The last band at $\tilde{\nu} \approx 3155 \text{ cm}^{-1}$ represents a combination of aromatic symmetric and asymmetric C–H bond stretching.

Many common features can be recognized in the spectra of N-free HTC and α -oligofurans. The vibrational spectrum of N-free HTC can be partially explained by the computed spectra of oligofurans up to $\tilde{\nu} = 1600 \text{ cm}^{-1}$ and in the region of aromatic C–H stretching. These findings are in agreement with analysis of IR spectra of several HTCs.^[40,45] For example, the sharp, strong band at $\tilde{\nu} \approx 1020 \text{ cm}^{-1}$ could be assigned to aromatic C–H scissoring, as in the case of α -oligofurans. Also, a weak band in the spectrum of N-free HTC at $\tilde{\nu} \approx 860 \text{ cm}^{-1}$ could be assigned to in-plane ring bending, which has a comparable position in the computed spectra of oligofurans. A wide group of bands in the region of $\tilde{\nu} = 1070\text{--}1470 \text{ cm}^{-1}$ in the spectrum of HTC could consist of a mixture of C=C and C–O stretching vibrations and C–H in-plane bending. However, the region in the range of $\tilde{\nu} = 1600\text{--}1800 \text{ cm}^{-1}$, the band at $\tilde{\nu} \approx 2950 \text{ cm}^{-1}$, and a broad band above $\tilde{\nu} = 3150 \text{ cm}^{-1}$ in the spectrum of N-free HTC cannot be explained by the pure oligofuranic structure. Despite many similarities between the computed oligofuran spectra and the experimental spectrum of N-free HTC, the intensities of the corresponding bands

cannot be compared because the spectrum of HTC is a combination of many overlapping vibrations. Furthermore, the bands of the N-free HTC spectrum are, in general, broader, which indicates the richness in molecular entities and functional groups. Large parts of the observed N-free HTC spectrum are not accounted for by the heterocyclic model structures. Hence, aliphatic (hydrocarbons) moieties also need to be present.

Comparison of the vibrational spectrum of N-free HTC and additional structures

Polyfurans can contain additional structural motifs to furan chains; these are described in detailed elsewhere.^[46] Similar motifs might be present in HTCs. Therefore, to assess how different functional groups influence the IR spectra of furans, we performed vibrational analysis on structures found in a review,^[46] and compared them with the experimental spectra of terfuran and N-free HTC (Figures 10 and 11). Analysis of

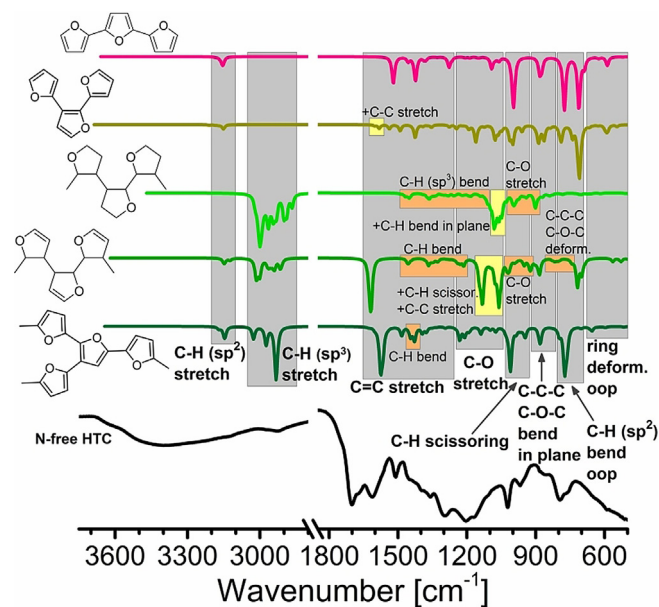


Figure 10. Computed vibrational spectra of additional structural motifs found in polyfurans and experimental FTIR spectrum of N-free HTC (black line).

computed spectra of these structural motifs shows that the N-free HTC contains aliphatic moieties. The vibrations of the sp^3 -carbon structure overlap with aromatic bands (regions of terfuran bands). The characteristic band from the spectrum of the 2,3-dihydrofuran moiety is C=C bond stretching at $\tilde{\nu} \approx 1620 \text{ cm}^{-1}$, which demonstrates that alkene-type motifs are present in the structure of HTCs. Also, other bands that represent nonaromatic C–H bond bending and stretching, as well as C–C bond stretching, could be present in N-free HTC, for instance, C–H scissoring from the spectrum of a dihydrofuran unit. The band at $\tilde{\nu} \approx 2950 \text{ cm}^{-1}$ in the spectrum of HTC agrees with the $\text{C}(\text{sp}^3)\text{--H}$ stretching modes that are also present in the furanic structures shown in Figure 10. HTCs could also comprise branched furanic structures.

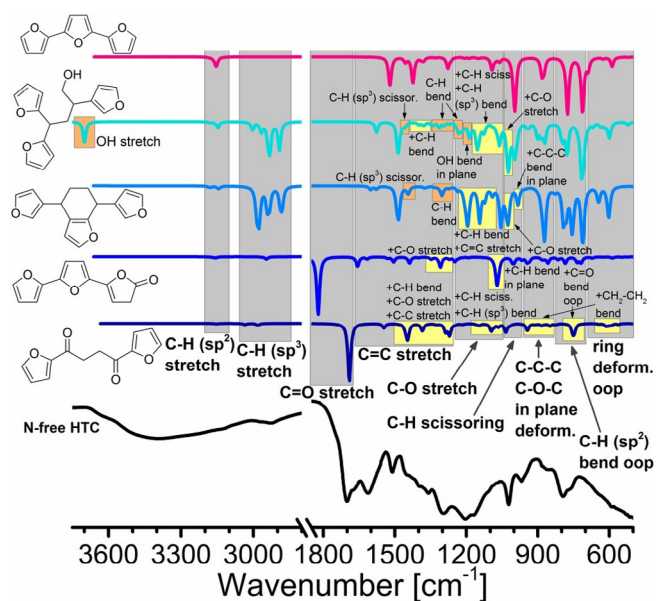


Figure 11. Computed vibrational spectra of additional structural motifs found in polyfurans and experimental FTIR spectrum of N-free HTC (black line).

Additional bands appear in the IR spectra of furanic moieties presented in Figure 11. They correspond mostly to C–H bending of both sp^2 - and sp^3 -carbon atoms, but carbonyl stretching bands of ketone and lactone may also be present.

Thermal analysis of HTC

Thermal analysis of the synthesized HTCs was performed under an argon atmosphere with a heating rate of 20 K min^{-1} .

Results of thermogravimetric (TG) studies of the HTCs are shown in Figure 12. For an N-free HTC char, approximately 50% mass loss can be observed. The highest mass loss of around 55% was determined for the sample with the highest N content (1:4 G/Uro), with a mass loss of 46% for the sample with the lowest N content (1:0.17 G/Uro). Among the synthesized HTC samples, the one with the lowest N content is more resistant to thermal decomposition. Conversely, the HTC sample with the highest N content is the one with lowest resistance to thermal degradation. All HTC chars show the same curve progression, with a similar decomposition process. It seems that mass loss depends, on the one hand, on the

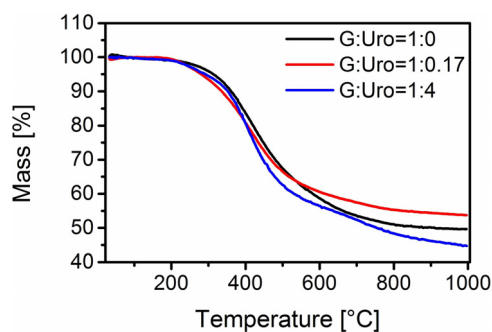


Figure 12. TG curves plotted as a function of temperature for 1:0, 1:0.17, and 1:4 G/Uro.

degree of internal condensation of the polymeric carbonaceous network structures and, on the other hand, on the functional groups. The recorded mass spectra of the decomposition products of the functional groups are shown in Figure 13. A higher degree of internal condensation results in more thermally stable HTC chars, as proved by the N-free sample. The N-HTC with the highest N content exhibits the highest mass loss, which is accounted for by the multitude of more thermostable N-functional groups that evolve strongly at approximately 800°C .

An unambiguous evaluation is aggravated by the fact that MS signals of N-functional groups overlap with signals of the O-functional groups. The recently developed isothermal segregation procedure and semiquantitative analysis of the O-functional groups could therefore not be applied.^[47] Nevertheless, trends within the synthesized HTCs can be determined. In accordance with the IR spectra, N-HTCs indicate lower abundance of oxygen-containing functional groups, as seen by a decrease in total intensities of the CO , CO_2 , and H_2O MS signals, relative to those of pure HTC.

The CO_2 (m/q 44) MS signals are caused by the thermal decomposition of carboxylic, lactone, and anhydride groups. They are present in all synthesized HTCs, but the total amount decreases with increasing N content and the ratio also changes. A shift in signal from around 389°C for pure HTC to around 341°C , and the appearance of a second signal at around 210°C for the N-HTCs can be observed. The ratio shifts towards more carboxylic and lactone groups than anhydrides.

This corresponds very well with the detected water signals (m/q 18). As a result of the abundance of hydrophilic function-

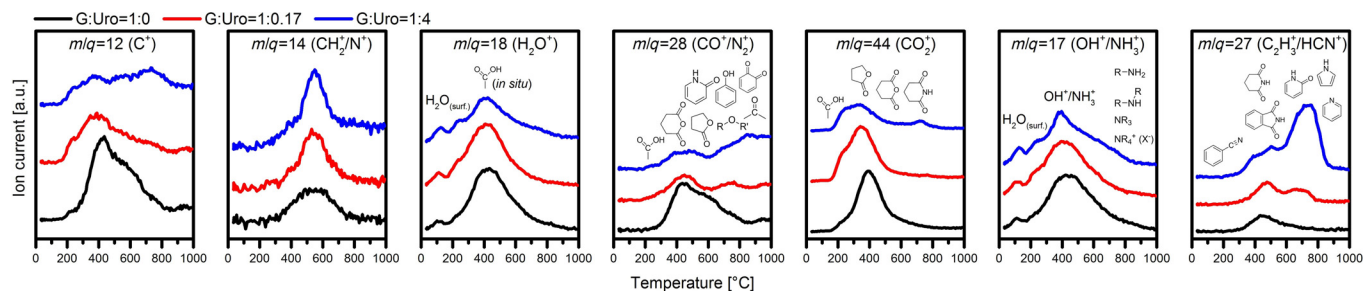


Figure 13. MS signals from TG-MS experiments plotted versus temperature. A vertical offset was applied for better comparability of N-free (black) and N-containing HTCs, depicting molar ratios of G and Uro with lowest (red) and highest N contents (blue).

al groups, bonded surface water desorbs at around 125 °C. Again, the total water signal is higher in the case of pure HTC than those for the N-containing samples. The signal of physisorbed water is superimposed by an intense water signal that arises at higher temperatures, around 411 °C, due to the evolution of water from neighboring carboxylic acid functional groups and the formation of anhydrides. Due to the intense water signal, it can be assumed that a high fraction of anhydride groups forms during the heating process from adjacent carboxylic groups, instead of being present directly after the synthesis. Therefore, the higher ratio of carboxylic groups in the N-HTC determined by the CO₂ signal is only ostensible due to broad distribution; this means that dehydration and transformation into anhydrides are hindered.

The detected mass of *m/q* 28 is representative for CO and N₂. The maxima of signals of pure and low N-containing HTC correspond very well with the maxima observed at *m/q* 18 (H₂O) and 44 (CO₂); these values again indicate anhydride groups. Further CO-releasing functional groups with higher thermal stability are phenols, ether, and carbonyl groups. These functions result in the shoulders observable for pure HTC at higher temperatures. With increasing N content of the HTCs, two fused peaks at 380 and 500 °C become dominant, most likely they can be attributed to N-containing functional groups because they do not appear in the pure HTC sample. In combination with the signals of *m/q* 27, they can be related to aromatic N-heterocycles, aromatic amines, or nitriles. Increasing signal intensities with increasing N content indicate that these are N-containing functional groups, rather than terminal vinyl derivatives (–C₂H₃). An indication of the existence of lactams is in situ decarbonylation to pyrrole groups, which can be found in the mass spectrum of CO⁺ at approximately 450–540 °C.^[48] The CO signal at 500 °C can be ascribed to this conversion. The stable intermediate, pyrrole, is supposed to decompose at around 680 °C with the release of HCN as seen at *m/q* 27.^[48c,49] Degradation of imide occurs through decarboxylation (*m/q* 44) of phthalimide at 450 °C,^[48c,50] yielding benzonitrile. Subsequently, benzonitrile decomposes to HCN at 500 °C, as inferred from the detection of a signal at *m/q* 27.^[48c,51] In contrast, pyrolysis of succinimide leads to the evolution not only of CO₂ and HCN, but also to the generation of isocyanic acid (HNCO) or isocyanate (NCO[–]) as key gaseous compounds.^[48c,52] The evolution of CO₂ can be observed at approximately 450 °C, analogous to imide decarboxylation. Exact determination is therefore complicated. The degradation to HNCO or NCO[–] occurs at around 510 °C. In the mass spectra of HNCO⁺ (*m/q* 43) and NCO⁺ (*m/q* 42) at 510 °C, it seems reasonable to suppose that the evolution of these gaseous products occurs (Figure S20 in the Supporting Information).

If the molar ratio of Uro to G is increasing (1:0.17 and 1:4 G/Uro), HCN and H₂ are released as gaseous pyrolysis products of pyrrole, as seen in the mass spectrum of HCN⁺ at 785 °C and in the H₂⁺ curves (*m/q* 2) at 805 °C (Figure S20 in the Supporting Information). Likewise, decomposition of the pyridinic groups generates HCN and H₂, which are formed at 905 and 920 °C, respectively.^[53] However, clear proof cannot be given for the origin of these signals, considering that pyrroles and

pyridines are only generated by samples containing a significant amount of nitrogen.

The detected signals of *m/q* 17 support the previous conclusions. The first maxima correlate with the signals of *m/q* 18, in terms of temperature and intensity, and are therefore attributed to OH⁺ resulting from water fragments. Additional signal intensities determined for *m/q* 17 at around 400 °C are associated with an overlap of OH⁺ ions and N-containing fragments. With increasing N content, the signals caused by H₂O become less dominant. The signal shapes become sharper and shift slightly to lower temperatures. The shoulder at around 680 °C becomes pronounced with increasing N content and can thus be ascribed to NH₃⁺ of amines.

The spectrum at *m/q* 12 of a N-free HTC sample exhibits a broad and a sharp signal between 175 and 845 °C. With increasing N content, this channel becomes less intense because N becomes the dominant species; this is confirmed by the signal of *m/q* 14. In the case of an N-free HTC char, the signal is broad but small within a temperature window between 309 and 761 °C. Herein, only methylene-type linkages (CH₂⁺) occur. As the N content increases, this signal shortens and becomes more pronounced. This can be accounted for by a synergetic interaction of N- and methylene-like connectivities.

Surface analysis

Zeta-potential measurements were performed as a function of pH for the synthesized HTCs in aqueous solution (Figure 14). Pure HTC shows completely negative zeta-potential values and no isoelectric point (IEP) over the measured pH range, as a result of the richness of acidic oxygen functional groups. The

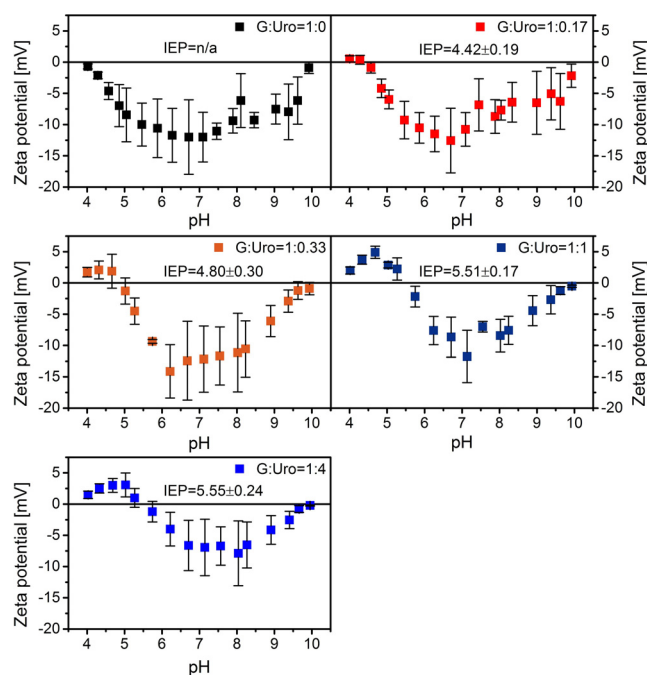


Figure 14. Zeta-potential measurements for HTCs derived from 1:0 (pure HTC, black), 1:0.17 (low N content, red), 1:0.33 (orange), 1:1 (dark blue), and 1:4 G/Uro (high N content, blue) as a function of pH.

lowest negative zeta-potential value is around -12 mV at around pH 6.7.

With increasing incorporation of nitrogen, an increase of the IEP from $\text{pH } 4.42 \pm 0.19$ to 5.55 ± 0.24 can be observed. Simultaneously, the negative zeta-potential values increase to more positive values from -12 to -6.6 mV at pH 6.7; this indicates that more basic functional groups or more functional groups with positive charge exist on the surface. This observation supports all aforementioned conclusions from FTIR spectroscopy, TG-MS, and acid–base titrations (Figure S21 in the Supporting Information).

Raman spectroscopy

The amorphous nature of the polymeric carbonaceous network of the HTCs broadens the two characteristic bands in the Raman spectra at $\tilde{\nu} = 1358$ and 1577 cm^{-1} through molecular excitations (Figure 15 and Figure S22 in the Supporting Infor-

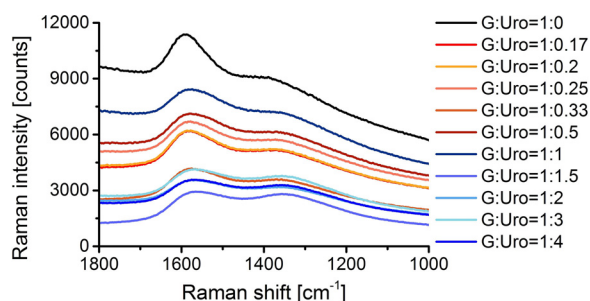


Figure 15. Cropped Raman spectra of all synthesized HTCs at different molar ratios of G/Uro for the region $\tilde{\nu} = 1000\text{--}1800 \text{ cm}^{-1}$. The fluorescence background indicates the polycyclic molecular structure of the HTCs.

mation).^[31] Although in the literature it is common to assign these two representative bands to the first-order Raman signals, the D and G bands,^[54] in this case, it is not possible because HTC chars are not of graphitic or graphene origin. The origin of soot can also be excluded because it can be denoted as a highly disordered graphitic structure.^[55] Hexabenzocoronene, which is referred to as a polycyclic aromatic hydrocarbon, cannot be compared because it is described as a graphene layer section and serves as a model for the building blocks of tiny graphitic domains, for example, in soot.^[55] Usually, the D band occurs as a result of the breathing modes of six-membered aromatic rings of phonons of A_{1g} symmetry, with disorder and defects in the graphitic or graphene lattice (e.g., edges/boundaries, sp^3 -carbon bonds, bonding disorders, vacancies, or heteroatoms).^[54–56] Thus, it highlights structural defects in the graphene layer.^[54] In contrast, the G band is ascribed to an “ideal”, ordered, undisturbed, sp^2 -bonded graphitic carbon lattice (chain or ring configurations)^[55,56c] that stems from the doubly degenerate zone center phonon E_{2g} mode.^[54] Likewise, the broad and weak band at $\tilde{\nu} \approx 2834 \text{ cm}^{-1}$ (Figure S21 in the Supporting Information) is neither attributed to a second-order 2D band (D-band overtone), which normally features few-layered graphene,^[54] nor accounted for combina-

tions of the G and D (G+D) graphitic lattice vibration modes, which are characteristic for disturbed graphitic structures.^[54,55] All in all, D, G, 2D, and combined G+D bands provide information about structural defects within graphitic systems.^[54,55] Therefore, detailed analyses, by applying different fitting methods, to obtain insights into the defect entities were not successful because these fitting methods were developed for graphitic or soot materials.^[47,55] XRD patterns of the measured HTC samples support the absence of highly structured domains due to a very broad band at around $10\text{--}20^\circ$ (Figure S23 in the Supporting Information).

There is also the effect that, due to the fluorescence background, a reasonable evaluation of the Raman spectrum is tremendously complicated. This phenomenon has been described before as an indication of the polycyclic molecular structure of carbon materials.^[31] Raman measurements were performed on different spots of the surface of the pellets. Low laser power, between 0.5 and 1.0 mW, was applied to avoid beam damage on the material surface. Depending on the spots measured, the intensity of the fluorescence changed; this indicates the inhomogeneity of the carbon structure of the HTCs. Annealing experiments would be appropriate to overcome this, but, at the same time, the amount of desired functional groups would be reduced. Nevertheless, for HTCs exhibiting acidic behavior, and thus, showing a uniformly black color, there is a change in the ratio of both bands. The band at $\tilde{\nu} = 1577 \text{ cm}^{-1}$ is sharper than the band at $\tilde{\nu} = 1358 \text{ cm}^{-1}$, which can be considered as evidence for a more condensed polymeric carbon network.^[31]

Electron energy-loss spectroscopy (EELS)

EELS is an efficient analytical characterization method for N-HTCs (Figure 16 and Figure S24 in the Supporting Information).

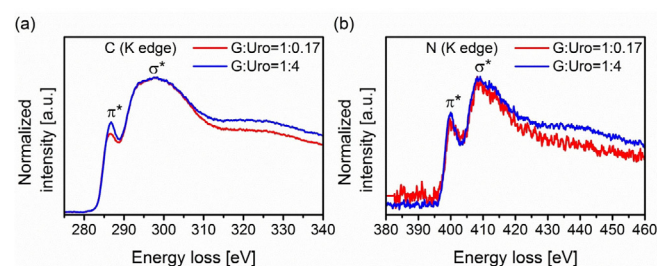


Figure 16. EELS spectra of N-HTCs with 1:0.17 and 1:4 G/Uro: a) C and b) N K edges.

The fine structure of the absorption band is related to bonding and the local electronic state.^[57] The spectrum reveals the representative excitation of the C 1s and N 1s shell electrons to the empty conduction band (Figure 16). The carbon K edge for both samples illustrates a sharp and defined band at 286.8 eV, which correspond to the excitation of 1s shell electrons to empty π^* orbitals.^[57b,58] For subsequent energy losses above 286.8 eV, the spectrum becomes smooth and featureless, which is characteristic of amorphous carbon.^[58a] Thus, the loss of long-range order leads to a collapse in dipole selection rules

and a blurring of the energy levels.^[58b] In addition, interatomic distances and linkages or cross-linking can no longer be determined.^[58a] The N-HTC can be referred to as an isotropic mixture of polycyclic compounds.^[58a] Transitions between 287 and 298 eV indicate a C–H σ^* orbital, and therefore, a high hydrogen content of both N-HTCs.^[58a,59] These findings were corroborated by Gaussian fitting of curves to the π^* and σ^* bands.^[58a,59a] Hence, the broad band at 293.4–301.8 eV cannot be ascribed to transitions to the π^* orbital interfusing partially with transitions to the σ^* orbital.^[58b] At this stage, the σ^* orbital is not yet fully defined.^[58a] It only occurs if the carbon materials are treated at higher temperatures, starting from around 750 °C.^[58a] However, the ratio between π^* and σ^* bands is often referred to as the degree of graphitization of the sample.^[57b] Consistent with this, the carbon K edge suggests an amorphous state with a mixture of both sp^2 and sp^3 hybridization for the N-HTCs. The EELS profile of carbon and nitrogen K edges are similar, which features the introduction of nitrogen atoms within the amorphous polymeric carbonaceous network. At around 399.9 eV, the π^* band in the nitrogen K edge is assigned to the sp^2 -hybridization state of N incorporated into the sp^2 -bonded carbon network.^[60] The σ^* band at approximately 408.5 eV is not only ascribed to the sp^3 -bonding nature with the carbon material, but also to defect sites within sp^3 bonding, such as pentagonal defects or corrugations within the structure.^[57a,61]

Structural comparison of different HTCs by solid-state NMR spectroscopy

N-free HTC (1:0 G/Uro, N: 0 wt%), a sample with the highest N content (1:4 G/Uro, N: 19 wt%), and a sample with the lowest N content (1:0.17 G/Uro, N: 7 wt%) were selected for NMR spectroscopy measurements. $^{13}C_6$ -labeled G and $^{13}C_6,^{15}N_4$ -labeled Uro were used as starting materials. Quantitative single-pulse direct polarization (DP) ^{13}C magic angle spinning (MAS)

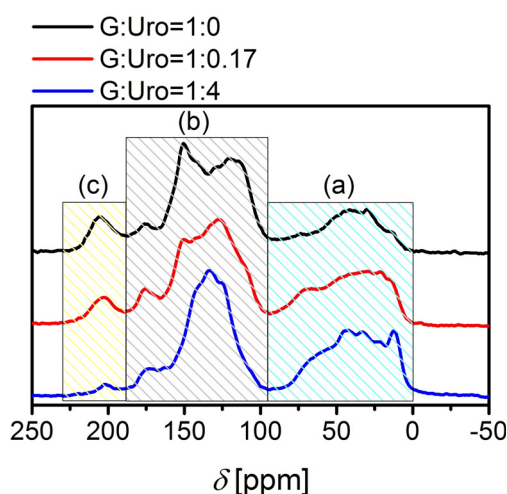


Figure 17. Quantitative DP ^{13}C NMR spectra of HTCs based on $^{13}C_6$ -labeled G and $^{13}C_6,^{15}N_4$ -labeled Uro for regions a) $\delta=0-95$, b) $95-188$, and c) $188-230$ ppm. Black: N-free HTC, red: lowest N-containing HTC, blue: highest N-containing HTC.

G/Uro	δ [ppm]	Functional group	Relative share [%]
1:0	188–230	ketone	9
	95–188	aromatic, carboxylic	65
	0–95	aliphatic	26
1:0.17	188–230	ketone	6
	95–188	aromatic, carboxylic	58
	0–95	aliphatic	36
1:4	188–230	ketone	2
	95–188	aromatic, carboxylic	55
	0–95	aliphatic	43

NMR spectroscopy experiments were performed on all three samples (Figure 17).^[62] The spectra can be divided coarsely into three regions. The sp^3 -aliphatic carbon atoms cover the chemical shift range from $\delta=0$ to 95 ppm (region a). Resonances of sp^2 -carbon atoms (C=C bonds), including aromatic and carboxylic groups, appear between $\delta=95$ and 188 ppm (region b). From $\delta=188$ to 230 ppm carbonyl groups, especially ketones and aldehydes, can be assigned (region c).^[24b,c,63] The quantification of the different regions for the three samples is summarized in Table 1.

The presence of aliphatic groups (region a) in the HTC structure increases from 26 to 43% with increasing N content. This can presumably be explained, on one hand, by the introduction of secondary amine groups, which show a resonance at $\delta \approx 53$ ppm (Figure 17), and, on the other hand, by the overall reductive synthetic conditions. At the same time, several resonances that correspond to sp^3 -aliphatic carbon atoms are rather well resolved at high N content, which indicates fairly well defined structural features. In particular, a resonance at $\delta=10$ ppm, which corresponds essentially to methyl groups connected to a carbon atom, shows an amplitude that indicates a relative share of about 5%. At low N content, this resonance is poorly resolved and less than half of the intensity; in the sample without N, its amplitude is reduced further. In addition, between $\delta=60$ and 90 ppm, there are overlapping resonances of different types of alkyl ether groups. Unreacted G would also show resonances in this region, yet the absence of noticeable signals between $\delta=90$ and 100 ppm indicates very low G content below about 1% relative share, even for N-free HTC.

The overall fraction of aromatic sp^2 -carbon atoms and C=C double bonds (Figure 17, region b) diminishes slightly from 65 to 55% with increasing N content, yet individual features change considerably. This region also includes sp^2 -carbon atoms with oxygen bonds, such as O–C=C or C=O groups (carboxylic acid moieties, carbonate, ester, amide) between $\delta=165$ and 185 ppm, heteroatom-bonded aromatic compounds ($\delta=145-165$ ppm), and aromatic compounds/acetals ($\delta=95-145$ ppm). The N-free HTC contains a small quantity of carboxylic acids. The proportion of furans is high and can be described by the signals at $\delta=110$ and 145 ppm. Through the addition of Uro (1:0.17 G/Uro), the share of carbon-based aromatic components rises, which corresponds to the resonance

at $\delta = 128$ ppm. Also, a high amount of methyl furan species can be identified at $\delta = 152$ ppm. For 1:4 G/Uro, the aromatic nature of the sample is by far the highest, as confirmed by the sharp signal at $\delta = 134$ ppm. The furan character of this HTC is quite low, probably due to substitution of O-functional groups with N-containing functional groups.

In region c (Figure 17), C=O groups, especially ketones and aldehydes ($\delta = 200$ – 220 ppm), can be detected. The ratio of carbonyl groups is highest for N-free HTC, with a share of 9%, and lowest for N-HTC with the highest N content, with a relative share of 2%; this can be accounted for by the reductive conditions during synthesis.

Cross-polarization (CP) MAS measurements with varying contact times were carried out for all three samples to determine C–H connectivities and to identify the chemical environment of ^{13}C and ^1H nuclei (Figure S25 in the Supporting Information). For the N-free HTC, weaker resonances are obtained beyond $\delta = 170$ ppm, which indicates a smaller concentration of aldehydes. In particular, HMF can be regarded as an aldehyde source. In the structural network, most heteroaromatic compounds are linked by C_α of a furan, whereas C_β features a high share of connected protons (Figure S25 in the Supporting Information).

For the lowest N-containing HTC, the presence of aldehydes can be excluded because resonances at characteristic frequencies do not show an enhancement at short contact times. For the signal at $\delta = 151$ ppm, the absence of bonded protons can be detected; this indicates cross-linking between C_α of the furan ring with, most likely, aliphatic carbon atoms. Similar to 1:0.17 G/Uro, in the highly N-containing HTC (1:4 G/Uro), the presence of aldehydes can also be excluded.

To identify carbon environments within a C–C network in the different structural motifs, 2D CP MAS homonuclear single-quantum double-quantum (SQ-DQ) ^{13}C correlation experiments were performed (Figure 18). The projections along F_1 and F_2 are compiled in Figures S26–S28 in the Supporting Information. The assignment of the cross-peaks of the correlation patterns to the corresponding C–C connectivity based on G or cellulose as starting materials is in accordance with the literature and can be found in detail elsewhere.^[24c,63,64]

For the N-free HTC, the broad cross-peak at $\delta = 12$ – 60 ppm (Figure 18, a) is derived from aliphatic carbon atoms, showing various C–C correlations among the aliphatic carbon atoms. Sharp correlations of C_α – C_β and C_β – C_β of furanic linkages are observed (f–g), but also furanic rings linked with aliphatic groups (b and c) and keto groups bonded with aliphatic compounds (Figure 18, d and e). The weak signals at $\delta \approx 176$ ppm (d) corroborate the presence of aliphatic carboxylic acids or esters. However, they can also be attributed to embedded or cross-linked levulinic acid type functions within the organic polymer-like carbonaceous network.^[24c,63a]

With respect to N-HTCs, additionally, ether-like functions (Figure 18, h) or pyrrolic-like groups can be proposed (i). In general, with gradually increasing N content, changes occur in the correlation spectra upon comparing a) with b) and c) in Figure 18. In particular, O-functional groups or atoms are substituted for N groups, which are observed from the occurrence

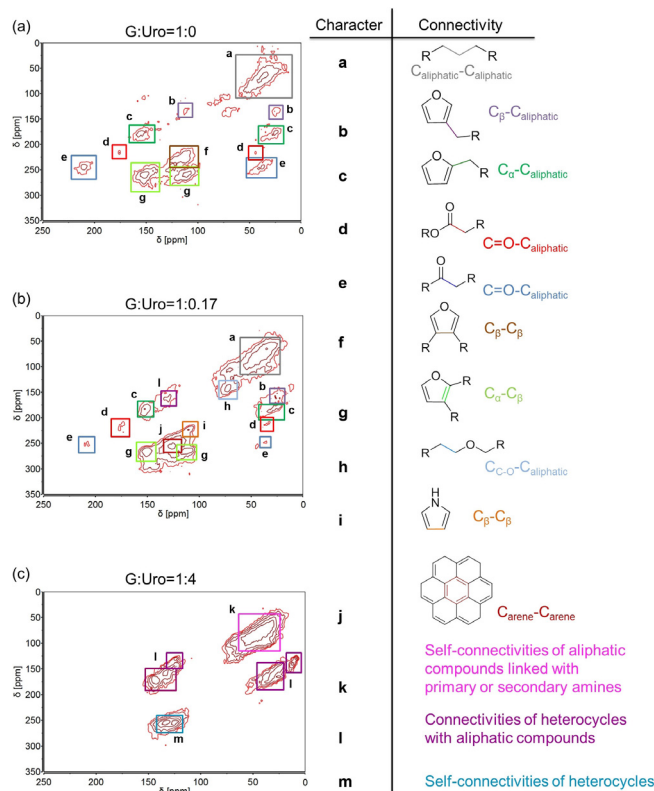


Figure 18. 2D CP MAS SQ-DQ ^{13}C correlation spectra, with 15 kHz spinning frequency, for a) 1:0, b) 1:0.17, and c) 1:4 G/Uro. Different resonances are marked with letters a–m. The corresponding structural motifs are shown on the right.

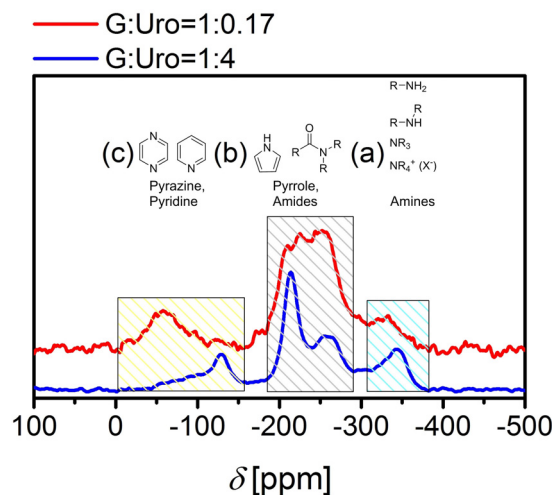


Figure 19. ^{15}N CP MAS NMR spectrum, with 30 kHz spinning frequency, for 1:0.17 (red) and 1:4 G/Uro (blue).

of correlation signals, such as i (Figure 18). The correlation spectrum of the N-HTC with 1:0.17 G/Uro reveals a rise of the aromatic carbon density, and an increase of aromatic self-connectivities into a polycyclic aromatic-like structure can be observed (Figure 18, j). Furthermore, connectivities of heterocyclic compounds with aliphatic compounds can be identified (l).

The correlation spectrum of the N-HTC with 1:4 G/Uro shows self-connectivities (C–C) of aliphatic compounds

bonded to primary or secondary amines (Figure 18, k). Likewise, the percentage of self-connectivities of heterocycles also increases (m). On the other hand, the cross-connectivities between carbonyl-based and aliphatic carbon atoms, as well as furanic rings, disappear completely. Instead, the share of N-functional groups and structural motifs rises. In addition to structural motifs such as pyrazine, pyridine, pyrrole, amides, or amines shown in Figure 19, further N-based compounds are possible.

Because the cross-peak (Figure 18, m) encloses a chemical shift between $\delta = 121$ and 137 ppm, according to reports in the literature, various structural motifs could be responsible. These include mainly five- and six-membered heterocyclic compounds. Among other heterocycles, imidazole is assumed to be a representative candidate, but further studies are necessary.^[65] Taken as a whole, the results prove that, in the absence of N, furanic structures are the essential structural motifs in which aliphatic compounds act as linkers within the polymeric carbon network. However, by increasing the molar ratio of Uro to G, furanic groups disappear due to the more reductive synthetic conditions and are substituted by N-containing entities.

The N-HTCs (1:0.17 and 1:4 G/Uro) were subjected to ¹⁵N CP MAS NMR spectroscopy measurements (Figure 19) to gain a detailed insight into N-functional moieties. As a chemical shift reference, the nitromethane scale was applied ($\delta_{\text{NH}_3} = \delta_{\text{CH}_3\text{NO}_2} + 380.5$ ppm).

Several N-containing structural motifs, such as amines, pyrrole, and amides, or pyrazine and pyridine (Table 2), can be as-

Table 2. Chemical shift assignments and structural motifs of the ¹⁵ N CP MAS NMR spectrum for 1:0.17 and 1:4 G/Uro.			
G/Uro	δ [ppm]	Structural motif	Region
1:0.17	-369 to -307	amines	a
	-290 to -185	pyrrole, amides	b
	-112 to -3	pyrazine, pyridine	c
1:4	-383 to -307	amines	a
	-290 to -185	pyrrole, amides	b
	-158 to -39	pyrazine, pyridine	c

signed to the resonances contained in distinct regions a–c (Figure 19). Mainly in regions b and c, considerable differences in the positions and shape of the resonances are visible for the two investigated N-HTCs. In general, for 1:0.17 G/Uro, the resonances are less clearly resolved than those for 1:4 G/Uro, which is consistent with a higher structural ordering with increasing N content, as already observed in the ¹³C NMR spectra. In region b, fewer resonances are visible for 1:4 G/Uro, which indicates a smaller number of distinct N-containing structural motifs. In region c, the main signal for 1:4 G/Uro appears at a lower resonance frequency than that for 1:0.17 G/Uro, which indicates a decrease in pyrazines and a simultaneous increase in pyridines with increasing N content. In region a, a distinction between primary, secondary, or tertiary amines is not unambiguously possible. As a rough trend, a small shift to-

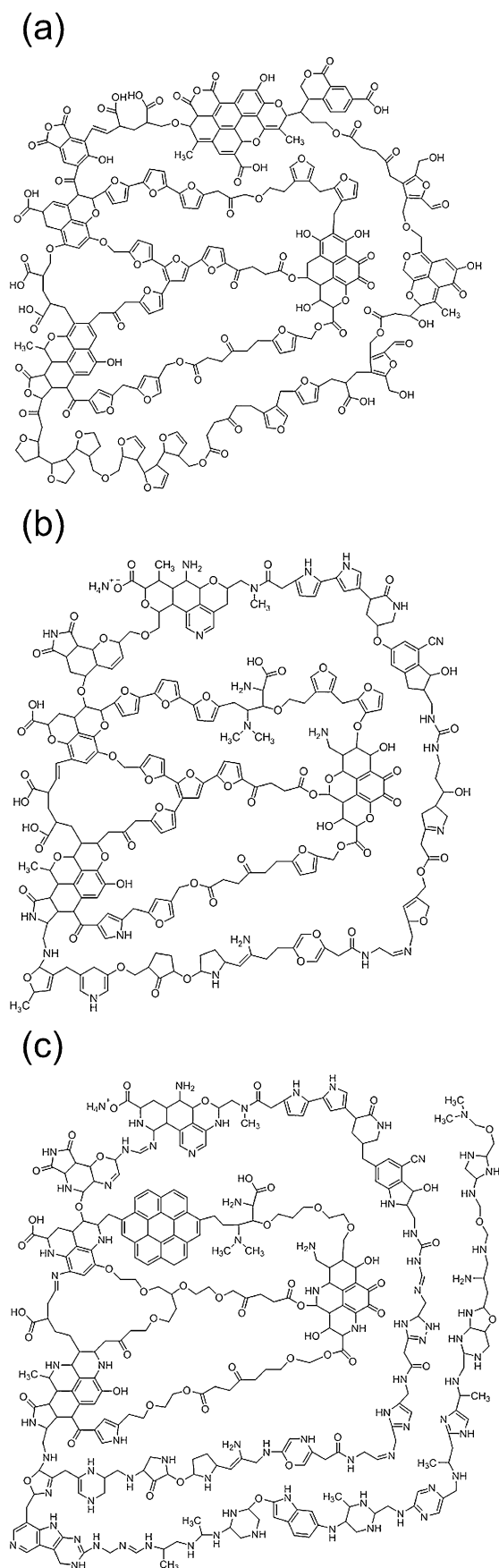


Figure 20. Structural models proposed for HTCs with a) N-free, b) lowest N-containing (7 wt%), and highest N-containing (19 wt%) scaffolds.

wards lower frequency for 1:4 G/Uro may indicate amides with more directly bound hydrogen atoms with increasing N. For the N-HTC with the highest N content, probably the quaternary amine with a resonance at $\delta = -343$ ppm can be assigned to an ammonium ion (NH_4^+).^[66]

Structural models

From the obtained results of elemental analysis, experimental and calculated FTIR spectra, TG-MS measurements, and solid-state NMR spectroscopy experiments, three different prototypical structural models are proposed to describe N-free (0 wt% N), lowest N-containing (7 wt% N), and highest N-containing (19 wt% N) HTCs (Figure 20). First, the carbon scaffold is considered to be a polymer-like structure, consisting of condensed cyclohexane and linear structures, as well as polyfuranic chain entities with only a few domains of aromaticity. Based on solid-state NMR spectroscopy results, the sp^2 -bonding character increases gradually with increasing N content; this implies that the aromatic nature of 1:4 G/Uro is highest. Simultaneously, aliphatic sp^3 -carbon atoms increase with an increasing amount of nitrogen. Hence, N-HTC with the highest N content (1:4 G/Uro) has the highest sp^3 character. The functional groups and structural motifs are taken on the basis of findings from FTIR spectra, TG-MS, and solid-state NMR spectra. Hydroxy, amine, methylene-type, and carbonyl groups, as well as aromatic alkene-like structures, are observed by FTIR spectroscopy. Further O-functional groups, such as carboxylic, anhydride, lactone, phenolic, ether, quinone, or keto groups, are determined based on TG-MS analysis. The N-functional groups, including nitrile, imide, lactam, amine (primary/secondary/tertiary/quaternary), pyrrolic, and pyridinic groups, are also attributed to TG-MS analysis. Both characterization techniques are surface-sensitive. Most information about functionalities or structural motifs is obtained from solid-state NMR spectroscopy, which is a bulk-sensitive analytical method; this involves aliphatic compounds (hydrocarbons), furanic entities (linked with aliphatic structures), aliphatic carboxylic acids or esters (embedded or cross-linked levulinic acid type functions), keto groups (bonded to aliphatic moieties), ether-like functionalities, and polycyclic condensed structures. In the presence of nitrogen, amide, amines (primary/secondary/tertiary/quaternary), pyrazine, pyrrolic, and pyridinic groups can be identified. Additionally, aliphatic carbon atoms bonded to primary or secondary amines and heterocycles (linked with aliphatic groups) can be detected. Based on the analysis of N-free HTCs, solely O-functional groups and O-related structural motifs are incorporated. Mainly furan-based entities bonded to aliphatic chains containing O atoms or groups such as levulinic acid type linkers are introduced. In addition, condensed cyclohexane rings or HMF moieties are taken into account (Figure 20a). The N-HTC with the lowest N content denotes a mixture of both O- and N-functional groups. Structural motifs include amine, amide, ammonium carboxylate, nitrile, amino acid, imide, lactam, and pyrrolic compounds (Figure 20b). The N-HTC with the highest N-containing scaffold exhibits a stronger percentage of the aforementioned N-functional groups, especially pyr-

rolic and pyridinic groups (Figure 20c). Therefore, we can conclude a successive exchange of O-functional groups by N-functional groups. Although carbonyl functional groups form furanic entities in the absence of N, the reaction pathways change with an increasing abundance of NH_3 in the reaction mixture, for instance, pyrrole or pyridine syntheses are favored. Hence, with only the addition of a large amount of N-precursor, more temperature-stable N-functional groups, such as pyrrole or pyridinic groups, are formed.

Conclusions

The hydrothermal synthetic route was applied based on the precursors G and Uro. Uro turns out to be a powerful N-precursor due to the multitude of possible reaction pathways it can undergo. In particular, its decomposition product, ammonia, contributes various reaction mechanisms, leading to numerous different structural motifs.

The HTC chars are semiconductor-like materials. The materials feature an extended degree of internal condensation of the polymeric carbonaceous network. Also, these materials possess a high powder density. It can be concluded that the combination of nitrogen and oxygen strengthen the stability of the structural network. Furthermore, the pronounced presence of the carbonyl group ($\text{C}=\text{O}$) is presumably an important factor for stabilization.

HTCs of spherical morphology with a high N content of about 19 wt% were achieved. Precursor decomposition during hydrothermal synthesis occurs over a wide range of complex reaction pathways, yielding a multitude of organic compounds, structural motifs, and functional groups, especially in the presence of an N-precursor. The preparative success results in HTC chars with a high number of N- and O-functional groups that are able to bind positively and negatively charged ions. The HTCs can therefore be used as adsorbents or for applications as supported catalysts. By increasing the molar ratio of Uro/G, the color of the materials turns from black to brown. Likewise, the HTC yield, carbon efficiency, and powder density of these N-HTCs diminish dramatically. The pH also changes to become more alkaline, which causes an increase in pyrrolic and pyridinic structural motifs, according to TG-MS experiments. Features such as the macroscopic morphology or internal polymeric structural network, which play a crucial role in the properties of the material, are drastically changed. By only adding a Uro mass fraction of about 3 wt%, the carbon efficiency could be increased to a maximum value of 64%, and a HTC yield of 42% could be reached.

This article is the first comprehensive analytical investigation of a series of N-containing HTCs, comprising analytical data obtained from UV/Vis spectroscopy, HPLC, optical microscopy, SEM/(HR)TEM, BET analysis, elemental analysis, FTIR spectroscopy, electronic structure calculations, TG-MS, zeta-potential measurements, acid-base titrations, Raman spectroscopy, XRD, EELS, and solid-state NMR spectroscopy. It was only through the combination of these methods that scientific findings on the complex structure could be obtained.

To assess the presence of certain functional groups or structural motifs from vibrational spectra, electronic structure calculations can be applied. Although the whole system is far too complex to simulate, the cooperative effects of different vibrational modes allow the estimation of the most abundant structural features of the carbonaceous network.

Solid-state NMR spectroscopy measurements confirmed that furan-based moieties were the key structural motifs in which aliphatic compounds acted as linkers within the polymeric carbonaceous network. By increasing the molar ratio of Uro/G, furanic structures disappeared due to the more reductive synthetic conditions and were substituted by N-containing entities.

The mechanistic success reflects on the three samples (Sample 1: 1:0 G/Uro, sample 2: 1:0.17 G/Uro, and sample 3: 1:4 G/Uro) that were subjected to solid-state NMR spectroscopy. Sample 1 follows the oxidative synthetic pathway, as described in Figure 1. Consequently, furan-based functions and condensed entities are obtained. Under these conditions, HTC chars with relatively low carbon efficiency are produced. Sample 2 probably first followed reductive and then oxidative synthetic routes. The final overall pH value is acidic. The O-functional groups are substituted by N-functional groups, but do not condense extensively into pyrrolic or pyridinic groups. The alkaline additive Uro seems to trigger an activating effect, in terms of chemical cross-linking of the polymeric carbonaceous network, to yield higher carbon efficiencies. Sample 3 was only exposed to alkaline medium during synthesis. Under these reductive conditions, a high proportion of fragmentation reactions occur, such as β -elimination, retro-aldol fragmentation, hydrolytic β -dicarbonyl fragmentation, benzoic acid type rearrangements, or deprotonations. These fragmentation reactions presumably again result in lower carbon efficiencies.

Three different structural models are proposed to describe N-free (0 wt% N), lowest N-containing (7 wt% N), and highest N-containing (19 wt% N) HTCs based on the findings of elemental analysis, experimental and calculated FTIR spectroscopy, TG-MS measurements, and solid-state NMR spectroscopy experiments. With increasing molar ratio of Uro/G, a gradual exchange of O-functional groups by N-functional groups can be induced. In the absence of nitrogen, mostly furanic entities linked to aliphatic groups are proposed. Through the addition of N-precursor, a multitude of parallel reactions occurs to form several types of N-functional groups and N-based structural motifs due to the increasing presence of NH_3 in the reaction mixture. Only with the addition of a high amount of N, more temperature-stable N-functional groups, such as pyrrole or pyridine, formed.

The suggested structural models are coal structure models, which are inspired by the diversity of existing coal structure models.^[67] Coal itself is one of the most heterogeneous organic sedimentary rocks of vegetal origin, with a complex chemical and physical structure, containing for the most part carbon; hydrogen; (hydro)aromatic rings; heteroatoms (O, N, or S); heterocycles (furan, quinone, pyridine, pyrrole, thiophene); aliphatic/ether bridges; and other elements, including mineral matter, which are cross-linked into a macromolecular three-di-

mensional network.^[67a–e,68] The structural models are therefore neither graphite nor macromolecules. Although HTC chars are somewhat similar to polymers, they can better be described as the lowest rank of coal. The rank of coal is correlated with the carbon content, heating value, and amount of volatile compounds. The lowest rank of coals are characterized by the lowest carbon content, lowest heating value, and highest amount of volatile compounds.^[69] Hence, HTC chars can be classified as lignite.^[70]

In carbon materials, heteroatoms, such as O or N, provide various advantages. In N-containing carbon, improved π bonding, electrical conductivity, and Lewis basicity are present; this simplifies reductive processes, such as reductive oxygen adsorption, on the carbon surface. Structural defects in the carbon lattice caused by heteroatoms yield more edge-active sites. It is accepted that edge-bound heteroatoms (e.g., pyridine) have an enhanced catalytic importance. The main advantage of the synthesized N-HTCs was that they were synthesized under mild reaction conditions, which provided them with polar surface functional groups responsible for their hydrophilic properties. This factor can modify their selectivity or can offer the possibility for further modifications by means of simple chemical functionalization.

Because HTC chars are regarded as green and sustainable renewable energy sources, one promising application is utilization in storage technologies, such as power-to-gas, converting electricity to hydrogen as a feedstock or fuel through water electrolysis, or producing carbon dioxide to generate synthetic natural gas (methanation).^[71] Among other applications, N-HTCs are promising candidates for utilization as sorption materials for the removal of heavy metals (Pb^{2+} , Cd^{2+} , Cu^{2+} , U^{6+}) or organic pollutants (e.g., dyes) from wastewater due to their abundance in surface functional groups. The low surface area of these materials does not present any problems. Through variation of the pH values, the selectivity towards a certain heavy metal could be increased by improving the binding capacity. Also, the removal of an organic dye pollutant from water can be achieved over a certain pH range. Overall, the obtained HTCs appear to be promising candidates for widespread applications in which the already mentioned advantageous properties of the materials might be of crucial importance. The materials are currently being tested for such applications. Ongoing works include further pressing the powder into pellets and subjecting them to pyrolysis to obtain disk electrode materials for electrochemical applications. Investigations include application in the water-splitting process within the oxygen evolution reaction (OER) or for fuel cell applications in the oxygen reduction reaction (ORR).

Experimental Section

Hydrothermal synthesis of N-functionalized carbon materials

All chemicals were of analytical grade. D-(+)-Glucose ($\geq 99.5\%$, GC) was purchased from Sigma Aldrich (Steinheim am Albuch, Germa-

ny). Hexamethylenetetramine ($\geq 99\%$) was supplied by Carl Roth Chemicals GmbH (Karlsruhe, Germany).

In a series of experiments, pure G (20 wt%, 7.71 g, 42.8 mmol) and a mixture of G and Uro were synthesized. First, only the mass fraction of G was changed and the mass fraction of Uro was kept constant. Samples with G (20 wt%, 7.71 g, 42.8 mmol, 1 equiv) and Uro (3 wt%, 1 g, 7.13 mmol, 0.17 equiv), as well as molar ratios of G/Uro of 1:0.2, 1:0.25, 1:0.33, 1:0.5, and 1:1, were synthesized. Additionally, in a second systematic series of experiments, only the mass fraction of Uro was varied and the mass fraction of G was kept constant. Samples with G (3 wt%, 1 g, 5.55 mmol, 1 equiv) and Uro (4 wt%, 1.17 g, 8.33 mmol, 1.5 equiv), as well as molar ratios of G/Uro of 1:2, 1:3, and 1:4, were prepared. The starting materials were dissolved in distilled water (30 mL) after intense stirring. The reaction mixtures were added to Teflon-lined stainless-steel autoclaves (50 mL volume). The autoclaves were then placed in a programmable laboratory oven preheated to 180 °C. After 6 h of reaction, the autoclaves were cooled to room temperature. After opening the autoclaves, the supernatants were gently collected separately for further analyses. The HTC's were removed from the autoclaves and recovered by filtration, washing several times with distilled water until the filtrate was colorless. The filter cakes were dried in an oven at 100 °C overnight. In an agate mortar, the HTC's were finally ground into powder.

Characterization

The liquid supernatant was analyzed by HPLC on an Agilent 1200 Series instrument with an ion-exchange column based on styrene divinyl benzene (REZEX™, RHM-Monosaccharide, 80 °C, injection volume: 5 μL , 0.6 mL min^{-1} , eluent: 0.005 M H_2SO_4). Measurements were automatically controlled by the Agilent ChemStation software. Compounds with more basic behavior, such as ammonia or amine compounds, could not be detected with the HPLC column. Potentiometric pH determination measurements from liquid supernatant were performed with a METTLER TOLEDO Titration Excellence T50 instrument with a universal METTLER TOLEDO DG 115-SC electrode (reference: ARGENTHAL TM, 0–100 °C, 0–14 pH); 60 s for each measurement. LabX light titration software v3.1 was used for automatic pH determination.

In situ UV/Vis diffuse reflectance (UV/VIS/near-IR) spectra were measured on a Cary Model 5000 spectrometer (Agilent) equipped with a Harrick Praying Mantis diffuse reflectance attachment (Model DRP-P72) and a solid-state in situ sample holder. Spectralon® was used as a white standard. Spectra were recorded over the range $\lambda = 200\text{--}2500$ nm with a step size of 0.5 nm every 0.1 s (scan rate: 300 nm min^{-1}) during the treatment of N-HTC's. The near-IR region was measured with a step size of 1 nm every 0.1 s (scan rate: 600 nm min^{-1}). Results were presented in the Kubelka–Munk function ($F(R_\infty)$) and Tauc function ($\{[F(R_\infty)]h\nu\}^{1/2}$) calculated from recorded reflectance data.

The HTC's were characterized by using a Thermo Scientific® Nicolet iS50 FTIR spectrometer equipped with an ATR diamond. To obtain a reasonable signal to noise (S/N) ratio, the samples were measured with 16 scans and a resolution of 4 cm^{-1} .

Elemental analysis was carried out by the external microanalytical laboratory Kolbe (Mikrolab Kolbe, Höhenweg 17, 45470 Mülheim an der Ruhr, Germany) by using a Vario EL CHNOS analyzer from the Elementar company.

Raman spectra were recorded by using a Thermo Scientific® DXR Raman microscope with 50 \times magnification and a $\lambda = 532$ nm laser with a laser power in the range of 0.5–1.0 mW. Samples were measured within 2 s and an exposure of 20 scans.

For SEM measurements, a Hitachi S-4800 field-emission scanning electron microscope was applied at 0.1–30 kV.

For (HR)TEM investigations, a FEI TITAN 80-300 instrument was used, working at acceleration voltages of 80, 200, and 300 kV. A JEOL JEM-ARM200F instrument was also applied, working at acceleration voltages of 80 and 200 kV.

TG-MS analyses were performed with the NETZSCH STA 449 F3 Jupiter® thermobalance setup connected to a quadrupole mass spectrometer (NETZSCH QMS 403 C Aëolos®). The sample was heated under an argon atmosphere with a constant gas flow of 50 mL min^{-1} over a temperature range of 40–1000 °C. For measurements, a temperature program with several isothermal steps was developed to separate the thermal decomposition events of distinct functional groups. A heating rate of 20 K min^{-1} was chosen to enable good signal separation and to avoid any effects of overheating. Corundum crucibles were filled with 14 mg of sample for measurements. Only the N-free HTC sample was used with another meas. Due to the low powder density, the crucible was filled to the brim with 8 mg of the N-free HTC.

Solid acid–base potentiometric titrations were conducted by using a METTLER TOLEDO Titration Excellence T50 instrument with a burette DV1020 dosing 1 μL of standard solutions (acid or base), including an error margin of 0.2%. A universal METTLER TOLEDO DG 115-SC electrode (reference: ARGENTHAL TM, 0–100 °C, 0–14 pH) recorded the pH automatically. LabX light titration software v3.1 was used to run the potentiometric titration automatically. First, HTC (100 mg) was dispersed in a 0.001 M solution of KCl (100 mL) and stirred overnight. The HTC sample was then titrated with a 0.01 M solution of HCl (20 mL). Afterwards, the acidified solutions were titrated with a 0.01 M solution of NaOH.

N_2 sorption experiments were recorded with an Autosorb 6-MP instrument (Quantachrome) at 77 K. Samples were outgassed between 7.5 and 10.5 h at 120 °C. Data were evaluated according to BET theory.

XRD measurements were performed in Bragg–Brentano geometry on a Bruker AXS D8 Advance II theta/theta diffractometer by using Ni-filtered $\text{Cu}_{\text{K}\alpha 1}$ radiation and a position-sensitive energy-dispersive LynxEye silicon strip detector. The sample powder was filled into the recess of a cup-shaped sample holder; the surface of the powder bed was flush with the sample holder edge (front loading).

Zeta-potential measurements were carried out by using a Zeta-PALS90 analyzer from Brookhaven Instruments Corporation provided with an autotitrator. Phase-analysis light scattering (PALS) was considerably more sensitive towards electrophoretic light scattering (ELS) method measured by conventional laser Doppler frequency shift. The PALS technique was able to detect the velocity of moving particles 100 times lower than that of the traditional ELS method. Hence, a higher precision was achieved to record the electrophoretic mobility (EPM). The phase shift was measured by using a $\lambda = 639$ nm laser. The current of the cell was automatically adjusted to approximately 2 mA. HTC (2 mg) was dispersed in distilled water (20 mL) in an ultrasonic bath for 10 min. To separate large particles, the dispersion was filtered with a 0.22 μm Rotilabo®-syringe filter (polyvinylidene fluoride (PVDF), unsterile). The HTC's were analyzed within a range of pH 3.2 to 10.2 adjusted with drops of 0.1 M KOH, 20 mM HNO_3 , and 1 mM HNO_3 .

To simulate the fundamental IR transitions of various model structures, geometry optimization and subsequent harmonic vibrational analysis was performed by means of DFT^[72] by employing the B3LYP^[73] functional in conjunction with the def2-TZVP basis set.^[74] The D3 dispersion correction by Grimme,^[75] with Becke–Johnson (BJ) damping,^[76] was used in all computations. Additionally, the RIJ-COSX^[77] approximation with corresponding auxiliary basis set^[78]

was applied. Computed harmonic vibrational frequencies were scaled by 0.97 to take into account anharmonicity. Because of the satisfactory agreement between experimental and scaled theoretical IR spectra of furan, a scaling factor of 0.97 was applied to other calculated vibrational spectra. Tight criteria were used for geometry optimization and self-consistent field (SCF) convergence. All calculations based on model compounds were performed by using the ORCA-4.0 suite of programs.^[79] Visualization of the molecular structures and Lorentzian band broadening for calculated spectra were prepared by using the ChemCraft program (version 1.7, programming: G. A. Zhurko; design, additional support: D. A. Zhurko; <https://www.chemcraftprog.com>) with about 14 a.u. of band width at half-height.

All NMR spectroscopy experiments were performed on a Bruker Avance III HD 400 MHz spectrometer with a 1.3 mm double-resonance MAS probe. The spinning frequency was 15 kHz for all CP experiments. For the single-pulse 1D experiments on ¹H and ¹³C, excitation $\pi/2$ pulses of 1.5 μ s at 15 and 70 W (v_{RF} = 166 kHz) with relaxation delays of 5 and 250 s were used, respectively. Ramped CP experiments with ¹H decoupling were able to achieve HH matching with the same power levels as those in the 1D experiments. The number of accumulations was 8 and 128 for ¹H and ¹³C, respectively. ¹⁵N CP experiments were performed at a spinning frequency of 30 kHz, with a power of 60 W and 2048 scans for sample 2 (1:0.17 G/Uro) and 9400 scans for sample 3 (1:4 G/Uro) with a delay of 5 s each.

¹³C DP measurements were conducted by applying 128 scans at a spinning frequency of 50 kHz to remove spinning side bands from the spectral region. The delay was set to 250 s to ensure complete relaxation.

¹³C 2D SQ-DQ correlation experiments were performed by utilizing the SC14 symmetry-based sequence^[23b] with simultaneous CP.^[23b] The power level requirement was met by using ¹H and ¹³C radiofrequency (RF) fields of approximately 52 and 100 kHz, respectively. An additional Lee–Goldburg offset on the ¹H channel was used to avoid HH contact during DQ generation and reconversion. The optimum signal was achieved by using 14 SC14 composite cycles for excitation and reconversion. Furthermore, 4096 and 128 points were used for the direct and indirect dimensions, respectively, and the number of accumulations was 400.

Both ¹H and ¹³C chemical shifts were referenced to adamantane (\geq 99%).

Acknowledgements

We would like to thank Jutta Kröhnert from the Fritz Haber Institute of the Max Planck Society for performing UV/Vis spectroscopic measurements, Wiebke Frandsen and Liudmyla Masliuk from the Fritz Haber Institute of the Max Planck Society for the recording of scanning and transmission electron micrographs, Frank Girgsdies from the Fritz Haber Institute of the Max Planck Society for XRD measurements, and Maike Hashagen from the Fritz Haber Institute of the Max Planck Society for carrying out BET measurements. A.A.A. and S.H. acknowledge funding from the MPG MAXNET Energy research initiative.

Conflict of interest

The authors declare no conflict of interest.

Keywords: biomass · carbon · hydrothermal synthesis · nitrogen · vibrational spectroscopy

- [1] a) J. Ming, Y. Wu, G. Liang, J.-B. Park, F. Zhao, Y.-K. Sun, *Green Chem.* **2013**, *15*, 2722–2726; b) S.-A. Wohlgemuth, F. Vilela, M.-M. Titirici, M. Antonietti, *Green Chem.* **2012**, *14*, 741–749.
- [2] M.-M. Titirici, *Sustainable Carbon Materials from Hydrothermal Processes*, 1st ed., Wiley, Chichester, **2013**.
- [3] a) J. A. Libra, K. S. Ro, C. Kammann, A. Funke, N. D. Berge, Y. Neubauer, M.-M. Titirici, C. Fühner, O. Bens, J. Kern, K.-H. Emmerich, *Biofuels* **2011**, *2*, 71–106; b) A. Gajić, H.-J. Koch, B. Märlander, *Sugar Ind.* **2011**, *136*, 791–799; c) A. Gajić, H.-J. Koch, *J. Environ. Qual.* **2012**, *41*, 1067–1075.
- [4] a) R. Z. Yang, X. P. Qiu, H. R. Zhang, J. Q. Li, W. T. Zhu, Z. X. Wang, X. J. Huang, L. Q. Chen, *Carbon* **2005**, *43*, 11–16; b) P. Kim, J. B. Joo, W. Kim, J. Kim, I. K. Song, J. Yi, *Catal. Lett.* **2006**, *112*, 213–218; c) Z. H. Wen, Q. Wang, Q. Zhang, J. H. Li, *Electrochem. Commun.* **2007**, *9*, 1867–1872; d) M. Sevilla, G. Lota, A. B. Fuertes, *J. Power Sources* **2007**, *171*, 546–551; e) J. B. Joo, Y. J. Kim, W. Kim, P. Kim, J. Yi, *Catal. Commun.* **2008**, *10*, 267–271; f) Z. H. Wen, Q. Wang, J. H. Li, *Adv. Funct. Mater.* **2008**, *18*, 959–964; g) Z. H. Wen, J. Liu, J. H. Li, *Adv. Mater.* **2008**, *20*, 743–747; h) M. Sevilla, C. Sanchís, T. Valdés-Solís, E. Morallón, A. B. Fuertes, *Electrochim. Acta* **2009**, *54*, 2234–2238; i) M. M. Tusi, N. S. de Oliveira Polanco, M. Brandalise, O. V. Correa, J. C. Villalba, F. J. Anaissi, A. O. Neto, E. V. Spinacé, *Int. J. Electrochem. Sci.* **2011**, *6*, 484–491.
- [5] a) Y.-S. Hu, R. Demir-Cakan, M.-M. Titirici, J.-O. Müller, R. Schlögl, M. Antonietti, J. Maier, *Angew. Chem. Int. Ed.* **2008**, *47*, 1645–1649; *Angew. Chem.* **2008**, *120*, 1669–1673; b) N. Brun, K. Sakaushi, L. Yu, L. Giebeler, J. Eckert, M. M. Titirici, *Phys. Chem. Chem. Phys.* **2013**, *15*, 6080–6087.
- [6] a) L. Zhao, L.-Z. Fan, M.-Q. Zhou, H. Guan, S. Qiao, M. Antonietti, M.-M. Titirici, *Adv. Mater.* **2010**, *22*, 5202–5206; b) C. Falco, J. M. Sieben, N. Brun, M. Sevilla, T. van der Maelen, E. Morallón, D. Cazorla-Amorós, M.-M. Titirici, *ChemSusChem* **2013**, *6*, 374–382.
- [7] a) N. Hedin, L. J. Chen, A. Laaksonen, *Nanoscale* **2010**, *2*, 1819–1841; b) L. Zhao, Z. Bacsik, N. Hedin, W. Wei, Y. H. Sun, M. Antonietti, M.-M. Titirici, *ChemSusChem* **2010**, *3*, 840–845; c) M. Sevilla, A. B. Fuertes, *Energy Environ. Sci.* **2011**, *4*, 1765–1771; d) M. Sevilla, C. Falco, M.-M. Titirici, A. B. Fuertes, *RSC Adv.* **2012**, *2*, 12792–12797.
- [8] a) Y. Yürüm, A. Taralp, T. N. Veziroglu, *Int. J. Hydrogen Energy* **2009**, *34*, 3784–3798; b) M. Sevilla, A. B. Fuertes, R. Mokaya, *Energy Environ. Sci.* **2011**, *4*, 1400–1410.
- [9] a) R. Demir-Cakan, N. Baccile, M. Antonietti, M.-M. Titirici, *Chem. Mater.* **2009**, *21*, 484–490; b) Z. G. Liu, F.-S. Zhang, *J. Hazard. Mater.* **2009**, *167*, 933–939; c) Z. G. Liu, F.-S. Zhang, J. Z. Wu, *Fuel* **2010**, *89*, 510–514; d) S. Kumar, V. A. Loganathan, R. B. Gupta, M. O. Barnett, *J. Environ. Manage.* **2011**, *92*, 2504–2512.
- [10] J. B. Zhou, C. Tang, B. Cheng, J. G. Yu, M. Jaroniec, *ACS Appl. Mater. Interfaces* **2012**, *4*, 2174–2179.
- [11] a) F. J. Xia, M. Pan, S. C. Mu, M. D. Jones, D. Wolverson, F. Marken, *Electroanalysis* **2012**, *24*, 1703–1708; b) W. B. Lu, X. Y. Qin, S. Liu, G. H. Chang, Y. W. Zhang, Y. L. Luo, A. M. Asiri, A. O. Al-Youbi, X. P. Sun, *Anal. Chem.* **2012**, *84*, 5351–5357.
- [12] a) X.-L. Li, T.-J. Lou, X.-M. Sun, Y.-D. Li, *Inorg. Chem.* **2004**, *43*, 5442–5449; b) C. H. Wang, X. F. Chu, M. M. Wu, *Sens. Actuat. B* **2007**, *120*, 508–513; c) Z. Guo, J. Y. Liu, Y. Jia, X. Chen, F. L. Meng, M. Q. Li, J. H. Liu, *Nanotechnology* **2008**, *19*, 345704.
- [13] a) B. R. Selvi, D. Jagadeesan, B. S. Suma, G. Nagashankar, M. Arif, K. Balasubramanyam, M. Eswaramoorthy, T. K. Kundu, *Nano Lett.* **2008**, *8*, 3182–3188; b) G. Gao, H. X. Wu, Y. X. Zhang, K. Wang, P. Huang, X. Q. Zhang, S. W. Guo, D. X. Cui, *J. Mater. Chem.* **2011**, *21*, 12224–12227; c) J. L. Gu, S. S. Su, Y. S. Li, Q. J. He, J. L. Shi, *Chem. Commun.* **2011**, *47*, 2101–2103.
- [14] a) Y.-P. Sun, B. Zhou, Y. Lin, W. Wang, K. A. S. Fernando, P. Pathak, M. J. Meziari, B. A. Harruff, X. Wang, H. F. Wang, P. J. G. Luo, H. Yang, M. E. Kose, B. L. Chen, L. M. Veca, S.-Y. Xie, *J. Am. Chem. Soc.* **2006**, *128*, 7756–7757; b) S.-R. Guo, J.-Y. Gong, P. Jiang, M. Wu, Y. Lu, S.-H. Yu, *Adv. Funct. Mater.* **2008**, *18*, 872–879; c) H.-W. Li, Y. Li, Y.-Q. Dang, L.-J. Ma, Y. Q. Wu, G. F. Hou, L. X. Wu, *Chem. Commun.* **2009**, 4453–4455.
- [15] M.-M. Titirici, A. Thomas, M. Antonietti, *New J. Chem.* **2007**, *31*, 787–789.

- [16] T. Y. Ma, L. Liu, Z. Y. Yuan, *Chem. Soc. Rev.* **2013**, *42*, 3977–4003.
- [17] a) S. Wohlgemuth, H. Urakami, L. Zhao, M.-M. Titirici, in *Sustainable Carbon Materials from Hydrothermal Processes*, 1st ed. (Ed.: M.-M. Titirici), Wiley, Chichester, **2013**, pp. 125–150; b) B. Hu, K. Wang, L. H. Wu, S.-H. Yu, M. Antonietti, M.-M. Titirici, *Adv. Mater.* **2010**, *22*, 813–828.
- [18] a) R. Arrigo, S. Wrabetz, M. E. Schuster, D. Wang, A. Villa, D. Rosenthal, F. Girsgdies, G. Weinberg, L. Prati, R. Schlögl, D. S. Su, *Phys. Chem. Chem. Phys.* **2012**, *14*, 10523–10532; b) Y. Xie, H. Li, C. Tang, S. Li, J. Li, Y. Lv, X. Wei, Y. Song, *J. Mater. Chem. A* **2014**, *2*, 1631–1635.
- [19] a) R. J. van Putten, J. C. van der Waal, E. de Jong, C. B. Rasrendra, H. J. Heeres, J. G. de Vries, *Chem. Rev.* **2013**, *113*, 1499–1597; b) E. F. L. J. Anet, *Adv. Carbohydr. Chem.* **1964**, *19*, 181–218.
- [20] a) C. J. Knill, J. F. Kennedy, *Carbohydr. Polym.* **2003**, *51*, 281–300; b) Z. Srokol, A.-G. Bouche, A. van Estrik, R. C. J. Strik, T. Maschmeyer, J. A. Peters, *Carbohydr. Res.* **2004**, *339*, 1717–1726.
- [21] a) D. J. Hayes, S. Fitzpatrick, M. H. B. Hayes, J. R. H. Ross, in *Biorefineries-Industrial Processes and Products: Status Quo and Future Directions, Vol. 1* (Eds.: B. Kamm, P. R. Gruber, M. Kamm), Wiley-VCH, Weinheim, **2006**, pp. 139–164; b) B. V. Timokhin, V. A. Baransky, G. D. Eliseeva, *Russ. Chem. Rev.* **1999**, *68*, 73–84; c) J. Horvat, B. Klaić, B. Metelko, V. Šunjić, *Croat. Chem. Acta* **1986**, *59*, 429–438; d) J. Horvat, B. Klaić, B. Metelko, V. Šunjić, *Tetrahedron Lett.* **1985**, *26*, 2111–2114.
- [22] S. K. R. Patil, C. R. F. Lund, *Energy Fuels* **2011**, *25*, 4745–4755.
- [23] a) N. Baccile, M. Antonietti, M.-M. Titirici, *ChemSusChem* **2010**, *3*, 246–253; b) N. Baccile, G. Laurent, C. Coelho, F. Babonneau, L. Zhao, M.-M. Titirici, *J. Phys. Chem. C* **2011**, *115*, 8976–8982; c) R. J. White, N. Yoshizawa, M. Antonietti, M.-M. Titirici, *Green Chem.* **2011**, *13*, 2428–2434; d) M. A. Glomb, in *Moderne Lebensmittelchemie*, 1st ed. (Eds.: M. Fischer, M. A. Glomb), Behr, Hamburg, **2015**, pp. 133–198.
- [24] a) M.-M. Titirici, R. J. White, C. Falco, M. Sevilla, *Energy Environ. Sci.* **2012**, *5*, 6796–6822; b) C. Falco, N. Baccile, M.-M. Titirici, *Green Chem.* **2011**, *13*, 3273–3281; c) N. Baccile, G. Laurent, F. Babonneau, F. Fayon, M.-M. Titirici, M. Antonietti, *J. Phys. Chem. C* **2009**, *113*, 9644–9654; d) E. Capuano, V. Fogliano, *LWT-Food Sci. Technol.* **2011**, *44*, 793–810; e) J. Koch, M. Pischetsrieder, K. Polborn, T. Severin, *Carbohydr. Res.* **1998**, *313*, 117–123; f) N. Baccile, J. Weber, C. Falco, M.-M. Titirici, in *Sustainable Carbon Materials from Hydrothermal Processes*, 1st ed. (Ed.: M.-M. Titirici), Wiley, Chichester, **2013**, pp. 151–212.
- [25] J. C. Sowden, *Adv. Carbohydr. Chem.* **1957**, *12*, 35–79.
- [26] a) I. Forsskåhl, T. Popoff, O. Theander, *Carbohydr. Res.* **1976**, *48*, 13–21; b) O. Theander, D. A. Nelson, *Adv. Carbohydr. Chem. Biochem.* **1988**, *46*, 273–326.
- [27] a) J. M. de Bruijn, A. P. G. Kieboom, H. van Bekkum, P. W. van der Poel, *Sugar Technol. Rev.* **1986**, *13*, 21–52; b) J. M. de Bruijn, A. P. G. Kieboom, H. van Bekkum, *Starch/Stärke* **1987**, *39*, 23–28; c) J. M. de Bruijn, F. Touwslager, A. P. G. Kieboom, H. van Bekkum, *Starch/Stärke* **1987**, *39*, 49–52; d) J. M. de Bruijn, A. P. G. Kieboom, H. van Bekkum, P. W. van der Poel, N. H. M. de Visser, M. A. M. de Schutter, *Int. Sugar J.* **1987**, *89*, 208–210; e) A. V. Ellis, M. A. Wilson, *J. Org. Chem.* **2002**, *67*, 8469–8474.
- [28] H. Steinhart, *Angew. Chem. Int. Ed.* **2005**, *44*, 7503–7504; *Angew. Chem.* **2005**, *117*, 7672–7673.
- [29] a) P. Buonora, J. C. Olsen, T. Oh, *Tetrahedron* **2001**, *57*, 6099–6138; b) R. Demir-Cakan, P. Makowski, M. Antonietti, F. Goettmann, M.-M. Titirici, *Catal. Today* **2010**, *150*, 115–118.
- [30] a) L. Liu, Q.-F. Deng, X.-X. Hou, Z.-Y. Yuan, *J. Mater. Chem.* **2012**, *22*, 15540; b) J. M. Dreyfors, S. B. Jones, Y. Sayed, *Am. Ind. Hyg. Assoc. J.* **1989**, *50*, 579–585.
- [31] S. Reiche, N. Kowalew, R. Schlögl, *ChemPhysChem* **2015**, *16*, 579–587.
- [32] a) A. B. Jorge, D. J. Martin, M. T. S. Dhanoa, A. S. Rahman, N. Makwana, J. Tang, A. Sella, F. Corà, S. Firth, J. A. Darr, P. F. McMillan, *J. Phys. Chem. C* **2013**, *117*, 7178–7185; b) Y. Li, J. Zhang, Q. Wang, Y. Jin, D. Huang, Q. Cui, G. Zou, *J. Phys. Chem. B* **2010**, *114*, 9429–9434.
- [33] a) J. Liu, Y. Liu, N. Y. Liu, Y. Z. Han, X. Zhang, H. Huang, Y. Lifshitz, S. T. Lee, J. Zhong, Z. H. Kang, *Science* **2015**, *347*, 970–974; b) X. C. Wang, K. Maeda, A. Thomas, K. Takanabe, G. Xin, J. M. Carlsson, K. Domen, M. Antonietti, *Nat. Mater.* **2009**, *8*, 76–80.
- [34] a) X. Li, J. Zhang, L. Shen, Y. Ma, W. Lei, Q. Cui, G. Zou, *Appl. Phys. A* **2009**, *94*, 387–392; b) C. Li, X. Yang, B. Yang, Y. Yan, Y. Qian, *Mater. Chem. Phys.* **2007**, *103*, 427–432; c) V. N. Khabashesku, J. L. Zimmerman, J. L. Margrave, *Chem. Mater.* **2000**, *12*, 3264–3270.
- [35] W. Rüetschi, Ph.D. thesis, Eidgenössische Technische Hochschule Zürich (Switzerland), **1941**.
- [36] a) V. K. LaMer, R. H. Dinegar, *J. Am. Chem. Soc.* **1950**, *72*, 4847–4854; b) A. Laaksonen, V. Talanquer, D. W. Oxtoby, *Annu. Rev. Phys. Chem.* **1995**, *46*, 489–524.
- [37] X. M. Sun, Y. D. Li, *Angew. Chem. Int. Ed.* **2004**, *43*, 597–601; *Angew. Chem.* **2004**, *116*, 607–611.
- [38] L. Zhao, N. Baccile, S. Gross, Y. Zhang, W. Wei, Y. Sun, M. Antonietti, M.-M. Titirici, *Carbon* **2010**, *48*, 3778–3787.
- [39] Z. Y. Liu, C. L. Zhang, L. Luo, Z. Chang, X. M. Sun, *J. Mater. Chem.* **2012**, *22*, 12149–12154.
- [40] L. H. Yu, C. Falco, J. Weber, R. J. White, J. Y. Howe, M.-M. Titirici, *Langmuir* **2012**, *28*, 12373–12383.
- [41] a) A. Kruse, A. Gawlik, *Ind. Eng. Chem. Res.* **2003**, *42*, 267–279; b) W. S.-L. Mok, M. J. Antal, *Ind. Eng. Chem. Res.* **1992**, *31*, 1157–1161.
- [42] E. Fuente, J. A. Menéndez, M. A. Díez, D. Suárez, M. A. Montes-Morán, *J. Phys. Chem. B* **2003**, *107*, 6350–6359.
- [43] R. J. White, C. Antonio, V. L. Budarin, E. Bergström, J. Thomas-Oates, J. H. Clark, *Adv. Funct. Mater.* **2010**, *20*, 1834–1841.
- [44] S. Glenis, M. Benz, E. LeGoff, J. L. Schindler, C. R. Kannewurf, M. G. Kanatzidis, *J. Am. Chem. Soc.* **1993**, *115*, 12519–12525.
- [45] M.-M. Titirici, A. Thomas, M. Antonietti, *J. Mater. Chem.* **2007**, *17*, 3412–3418.
- [46] M. J. González-Tejera, E. Sánchez de la Blanca, I. Carrillo, *Synth. Met.* **2008**, *158*, 165–189.
- [47] P. Dünge, M. Prenzel, C. Van Stappen, N. Pfänder, S. Heumann, R. Schlögl, *Mater. Sci. Appl.* **2017**, *8*, 628–641.
- [48] a) R. Arrigo, M. Hävecker, R. Schlögl, D. S. Su, *Chem. Commun.* **2008**, 4891–4893; b) S. Kundu, W. Xia, W. Busser, M. Becker, D. A. Schmidt, M. Havenith, M. Muhler, *Phys. Chem. Chem. Phys.* **2010**, *12*, 4351–4359; c) K. Friedel Ortega, R. Arrigo, B. Frank, R. Schlögl, A. Trunschke, *Chem. Mater.* **2016**, *28*, 6826–6839.
- [49] K.-M. Hansson, J. Samuelsson, L.-E. Åmand, C. Tullin, *Fuel* **2003**, *82*, 2163–2172.
- [50] J. Żurakowska-Orszagh, T. Chreptowicz, *Eur. Polym. J.* **1981**, *17*, 877–880.
- [51] a) K. Chen, J. C. Mackie, D. Wojtalewicz, E. M. Kennedy, B. Z. Dlugogorski, *J. Hazard. Mater.* **2011**, *187*, 407–412; b) Sonya-T-Emad-Rad, E. Metcalfe, *Fire Mater.* **1993**, *17*, 33–37.
- [52] a) G. Choudhary, A. M. Cameron, R. A. Back, *J. Phys. Chem.* **1968**, *72*, 2289–2292; b) D. J. Bogan, C. W. Hand, *J. Phys. Chem.* **1971**, *75*, 1532–1536.
- [53] a) X. Hong, L. Zhang, T. Zhang, F. Qi, *J. Phys. Chem. A* **2009**, *113*, 5397–5405; b) E. Ikeda, J. C. Mackie, *J. Anal. Appl. Pyrolysis* **1995**, *34*, 47–63; c) B. Xiao, J. P. Boudou, K. M. Thomas, *Langmuir* **2005**, *21*, 3400–3409.
- [54] Z. Xing, Z. C. Ju, Y. L. Zhao, J. L. Wan, Y. B. Zhu, Y. H. Qiang, Y. T. Qian, *Sci. Rep.* **2016**, *6*, 26146.
- [55] A. Sadezky, H. Muckenhuber, H. Grothe, R. Niessner, U. Pöschl, *Carbon* **2005**, *43*, 1731–1742.
- [56] a) R. Atchudan, T. N. J. I. Edison, S. Perumal, Y. R. Lee, *Appl. Surf. Sci.* **2017**, *393*, 276–286; b) M. Asadullah, S. Zhang, Z. Min, P. Yimsiri, C.-Z. Li, *Ind. Eng. Chem. Res.* **2009**, *48*, 9858–9863; c) M. Chhowalla, A. C. Ferrari, J. Robertson, G. A. J. Amaratunga, *Appl. Phys. Lett.* **2000**, *76*, 1419.
- [57] a) Y. M. Lin, X. L. Pan, W. Qi, B. S. Zhang, D. S. Su, *J. Mater. Chem. A* **2014**, *2*, 12475–12483; b) A. Braun, *J. Environ. Monit.* **2005**, *7*, 1059–1065; c) J. Robertson, *Semicond. Sci. Technol.* **2003**, *18*, S12–S19.
- [58] a) H. Daniels, R. Brydson, B. Rand, A. Brown, *Philos. Mag.* **2007**, *87*, 4073–4092; b) J. Bruley, P. Madakson, J. C. Liu, *Nucl. Instrum. Methods Phys. Res. Sect. B* **1990**, *45*, 618–621.
- [59] a) J. Stöhr, *NEXAFS Spectroscopy, Vol. 25*, Springer, Heidelberg, **1992**; b) G. Comelli, J. Stöhr, C. J. Robinson, W. Jark, *Phys. Rev. B* **1988**, *38*, 7511–7519.
- [60] J. Robertson, C. A. Davis, *Diamond Relat. Mater.* **1995**, *4*, 441–444.
- [61] C. Wang, Z. H. Huang, L. Zhan, Y. L. Wang, W. M. Qiao, X. Y. Liang, L. C. Ling, *Diamond Relat. Mater.* **2011**, *20*, 1353–1356.
- [62] J. A. Franz, R. Garcia, J. C. Linehan, G. D. Love, C. E. Snape, *Energy Fuels* **1992**, *6*, 598–602.
- [63] a) I. van Zandvoort, E. J. Koers, M. Weingarh, P. C. A. Brujininx, M. Baldus, B. M. Weckhuysen, *Green Chem.* **2015**, *17*, 4383–4392; b) J. D. Mao, X. Y. Cao, D. C. Oik, W. Y. Chu, K. Schmidt-Rohr, *Prog. Nucl. Magn. Reson. Spectrosc.* **2017**, *100*, 17–51.

- [64] C. Falco, F. Perez Caballero, F. Babonneau, C. Gervais, G. Laurent, M.-M. Titirici, N. Baccile, *Langmuir* **2011**, *27*, 14460–14471.
- [65] a) M. Begtrup, J. Elguero, R. Faure, P. Camps, C. Estopá, D. Ilavský, A. Fruchier, C. Marzin, J. de Mendoza, *Magn. Reson. Chem.* **1988**, *26*, 134–151; b) D. C. G. A. Pinto, C. M. M. Santos, A. M. S. Silva, in *Research Developments in Heterocyclic Chemistry* (Eds.: T. M. V. D. Pinho e Melo, A. M. d. A. Rocha Gonsalves), Research Signpost, Trivandrum, **2007**, pp. 397–475.
- [66] S. Hayashi, K. Hayamizu, *Bull. Chem. Soc. Jpn.* **1991**, *64*, 688–690.
- [67] a) J. A. Theron, E. le Roux, *J. South. Afr. Inst. Min. Metall.* **2015**, *115*, 339–348; b) M. S. Masoudian, D. W. Airey, A. El-Zein, *Geomech. Geoen.* **2013**, *8*, 229–243; c) M. W. Haenel, *Fuel* **1992**, *71*, 1211–1223; d) A. Marzec, *J. Anal. Appl. Pyrolysis* **1985**, *8*, 241–254; e) J. H. Shinn, *Fuel* **1984**, *63*, 1187–1196; f) D. G. Levine, R. H. Schlosberg, B. G. Silbernagel, *Proc. Natl. Acad. Sci. USA* **1982**, *79*, 3365–3370; g) W. H. Wiser, in *Proceedings of the Electric Power Research Institute Conference on Coal Catalysis*, Palo Alto, California, **1973**, pp. 3–53; h) P. H. Given, *Fuel* **1960**, *39*, 147–153.
- [68] M. R. Dong, X. L. Mao, J. J. Gonzalez, J. D. Lu, R. E. Russo, *J. Anal. At. Spectrom.* **2012**, *27*, 2066–2075.
- [69] a) B. J. Arnold, in *The Coal Handbook: Towards Cleaner Production, Vol. 1: Coal Production* (Ed.: D. Osborne), Woodhead, Sawston, **2013**, pp. 31–52; b) J. Hoinkis, E. Lindner, *Chemie für Ingenieure*, 13th ed., Wiley-VCH, Weinheim, **2007**.
- [70] a) A. Gajić, in *Einfluss von HTC-Biokohle auf chemische und physikalische Bodeneigenschaften und Pflanzenwachstum*, Institut für Zuckerrübenforschung, Göttingen, Germany, **2012**, pp. 1–10; b) H.-G. Ramke, D. Blöhse, in *Fachgespräch Feststoffuntersuchung 2010—Neue Entwicklungen in der Abfall- und Atlastenuntersuchung*, Bildungsstätte Essen des Bildungszentrum für Entsorgungs- und Wasserwirtschaft GmbH, Ministerium für Umwelt und Naturschutz, Landwirtschaft und Verbraucherschutz des Landes NRW, Essen, Germany, **2010**, pp. 1–21.
- [71] X. J. Zhang, C. Bauer, C. L. Mutel, K. Volkart, *Appl. Energy* **2017**, *190*, 326–338.
- [72] a) W. Koch, M. C. Holthausen, *A Chemist's Guide to Density Functional Theory*, 1st ed., Wiley-VCH, Weinheim, **2000**; b) R. G. Parr, W. Yang, *Density-Functional Theory of Atoms and Molecules*, Oxford University Press, New York, **1994**.
- [73] P. J. Stephens, F. J. Devlin, C. F. Chabalowski, M. J. Frisch, *J. Phys. Chem.* **1994**, *98*, 11623–11627.
- [74] F. Weigend, R. Ahlrichs, *Phys. Chem. Chem. Phys.* **2005**, *7*, 3297–3305.
- [75] a) S. Grimme, *J. Comput. Chem.* **2006**, *27*, 1787–1799; b) S. Grimme, J. Antony, S. Ehrlich, H. Krieg, *J. Chem. Phys.* **2010**, *132*, 154104.
- [76] a) A. D. Becke, E. R. Johnson, *J. Chem. Phys.* **2005**, *123*, 154101; b) E. R. Johnson, A. D. Becke, *J. Chem. Phys.* **2005**, *123*, 024101; c) E. R. Johnson, A. D. Becke, *J. Chem. Phys.* **2006**, *124*, 174104.
- [77] a) F. Neese, F. Wennmohs, A. Hansen, U. Becker, *Chem. Phys.* **2009**, *356*, 98–109; b) R. Izsák, F. Neese, *J. Chem. Phys.* **2011**, *135*, 144105.
- [78] K. Eichkorn, F. Weigend, O. Treutler, R. Ahlrichs, *Theor. Chem. Acc.* **1997**, *97*, 119–124.
- [79] F. Neese, *WIREs Comput. Mol. Sci.* **2012**, *2*, 73–78.

 Manuscript received: January 23, 2018

Revised manuscript received: March 19, 2018

Accepted manuscript online: March 25, 2018

Version of record online: May 2, 2018